Separating Atmospheric and Ocean-Mediated Impacts of Time-Evolving Industrial and Biomass Burning Aerosols on Historical Boreal Summer Climate

XUEYING ZHAO,[a,b] CLARA DESER,[a] GEETA PERSAD,[b] ADAM S. PHILLIPS,[a] KAYLA WHITE,[b] AND NAN ROSENBLOOM[a]

[a] *NSF National Center for Atmospheric Research, Boulder, Colorado*
[b] *Jackson School of Geosciences, The University of Texas at Austin, Austin, Texas*

(Manuscript received 22 October 2025, in final form 25 June 2026, accepted 10 July 2026)

ABSTRACT: The spatial pattern of industrial aerosol emissions has changed markedly over the past century, alongside regional shifts in biomass burning (BMB) sources. While previous studies examined evolving industrial aerosol effects, the relative contributions of atmospheric radiative versus ocean-mediated responses to combined aerosol sources remain unclear. Using global atmosphere–land simulations driven by time-evolving historical industrial and BMB aerosol emissions and aerosol-induced sea surface temperature (SST) anomalies, we identify two leading modes of multidecadal aerosol optical depth (AOD) variability in boreal summer, together accounting for 94% of the AOD variance from 1930 to 2030. Mode 1 depicts a monotonic increase over low latitudes, while mode 2 describes a sinusoidal trajectory over Northern Hemisphere continents with weaker opposite changes over South and East Asia. These AOD modes drive distinct atmospheric circulation, precipitation, and land surface air temperature responses. We separate the atmospheric radiative and ocean-mediated pathways of response through a novel experimental design based on Community Atmosphere Model, version 5, forced with time-evolving aerosol emissions and aerosol-induced SSTs individually and in combination; aerosol-induced SSTs are derived from the Community Earth System Model, version 1, Single-Forcing and All-Forcing Large Ensembles. We find that ocean-mediated effects dominate the large-scale atmospheric circulation and precipitation responses, while atmospheric radiative effects induce robust regional impacts and modulate the ocean-mediated response in remote regions. Our results demonstrate that transient aerosol impacts reflect a dynamic balance between atmospheric radiative and ocean-mediated pathways of response and highlight the importance of considering the evolving spatial pattern of aerosol forcing when assessing aerosol-driven climate variations.

SIGNIFICANCE STATEMENT: Aerosols from industrial activities and biomass burning have changed significantly over the twentieth century. We conduct a novel set of climate model simulations to investigate how the changing spatial distribution of these aerosol emissions influenced historical climate via atmospheric and oceanic pathways. Using a pattern-based approach, we find that these aerosols influence global climate by modifying ocean surface temperatures, which in turn drive changes in global-scale atmospheric circulation, affecting precipitation and land surface air temperature. Aerosols' interaction with radiation in the atmosphere drives local and regional impacts and modulates oceanic-driven responses in remote regions. Our results highlight the importance of evolving aerosol patterns in shaping historical anthropogenic climate change and underscore the complexity of atmospheric and oceanic pathways governing the responses.

KEYWORDS: Atmospheric circulation; Anthropogenic effects/forcing; Radiative forcing; Numerical analysis/modeling

1. Introduction

Aerosols from anthropogenic sources are one of the dominant drivers of climate change over the industrial era (IPCC 2021). Aerosols from industrial sources have played a key role in shaping historical patterns of forced climate change in the atmosphere and ocean, with impacts on regional temperature and precipitation (e.g., Dong et al. 2024; Shi et al. 2022; Kang et al. 2021; Deser et al. 2020; Xie et al. 2013). For instance, Northern Hemisphere (NH) industrial aerosol emissions have been linked to the observed southward shift of the tropical Pacific and Atlantic rain belts in the late twentieth century (Ming and Ramaswamy 2011; Hwang et al. 2013; Hill et al. 2015; Allen et al. 2015). Aerosols from industrial sources, including those at lower latitudes, have also contributed to the weakening of South and East Asian summer monsoon circulations and the associated decrease in monsoon precipitation (Bollasina et al. 2011, 2014), as well as Sahel drought and subsequent recovery (Hua et al. 2019; Hirasawa et al. 2020). Industrial aerosol emissions have also been implicated in the recent weakening of the NH summertime atmospheric circulation, including the upper-level jet stream (Dong et al. 2022) and storm tracks (Kang et al. 2024; Chemke and Coumou 2024). In addition, the historical NH midlatitude aerosol increase has been suggested to delay the emergence of Arctic amplification until the past few decades (Mueller et al. 2018; England et al. 2021), while their reductions after the 1980s

Denotes content that is immediately available upon publication as open access.

Supplemental information related to this paper is available at the Journals Online website: https://doi.org/10.1175/JCLI-D-25-0599.s1.

Corresponding author: Xueying Zhao, xueying.zhao@jsg.utexas.edu

DOI: 10.1175/JCLI-D-25-0599.1

© 2026 American Meteorological Society. This published article is licensed under the terms of the default AMS reuse license. For information regarding reuse of this content and general copyright information, consult the AMS Copyright Policy (www.ametsoc.org/PUBSReuseLicenses).

Unauthenticated | Downloaded 10/07/26 05:58 PM UTC

are linked to recent enhanced summer warming in western Europe (Schumacher et al. 2024; Roesch et al. 2025). Furthermore, industrial aerosol emissions, by modulating atmospheric radiation reaching the surface, have affected oceanic properties such as sea surface temperature (SST), sea surface salinity, and heat content (Shi et al. 2022; Dong et al. 2024), which in turn influence ocean heat uptake and heat exchange between basins (Li et al. 2023) and have delayed the formation of the "North Atlantic warming hole" (Dagan et al. 2020).

Biomass burning (BMB) emissions, another major partially anthropogenic source of aerosols, have coevolved with industrial emissions. However, the large-scale climatic impacts of BMB aerosols have received little attention until recently, due in part to incomplete inventories of historical BMB emissions (Hua et al. 2024) and BMB's relatively minor effect on the global mean energy balance (IPCC 2021). In addition, large uncertainties in BMB-driven aerosol–cloud interactions and their dependence on aerosol types have hampered progress (IPCC 2021). The recent acceleration of human-related wildfire worldwide has prompted renewed scrutiny of the role of BMB emissions in anthropogenic climate change (Cunningham et al. 2024). In particular, it has been demonstrated that BMB emissions reduce time-mean total aerosol radiative forcing (Heyblom et al. 2023), partially mitigating the effect of industrial aerosol emissions on the strength of the Atlantic meridional overturning circulation (AMOC; Allen et al. 2024; Liu et al. 2024) and accelerating externally forced twentieth century warming of the tropical Indian Ocean at a faster speed relative to other tropical ocean basins (Tian et al. 2023). In addition, interannual variations in BMB emissions have been shown to produce a sizeable effect on NH climate via nonlinear aerosol–cloud interactions, contributing to high-latitude warming and Arctic sea ice decline in recent decades (Fasullo et al. 2022; DeRepentigny et al. 2022).

Industrial aerosol and BMB emissions are spatially heterogeneous and have evolved substantially over time though with different spatiotemporal patterns. Industrial aerosol emissions are primarily located in the NH subtropics and midlatitudes, while BMB emissions mainly occur in the deep tropics and boreal regions (van der Werf et al. 2017). From the 1950s to the 1970s, industrial aerosol emissions increased rapidly over North America and western Europe, followed by marked declines resulting from clean air legislation (e.g., Deser et al. 2020). After the late 1970s, the locus of industrial aerosol emissions shifted to East Asia and South Asia. Following the passage of China's Air Pollution Prevention and Control Action Plan (Zhang et al. 2021), local industrial emissions dropped rapidly particularly after 2013 (Wang et al. 2021), shaping a dipole pattern between East and South Asia (Xiang et al. 2023). Meanwhile, tropical BMB emissions increased substantially over the second half of the twentieth century in central Africa, South America, and Southeast Asia due to agricultural activities and land-use changes (van der Werf et al. 2017). Boreal BMB emissions have also risen over the twentieth century, particularly in Siberia and parts of Canada (van der Werf et al. 2017).

The effect of radiative forcings such as aerosols can be decomposed into atmospheric radiative and ocean-mediated components. These are commonly referred to as "fast" and "slow" responses, respectively, reflecting the time scales over which they appear, where fast denotes the response in the absence of significant surface temperature changes and slow denotes the surface temperature feedback response (Gregory et al. 2004; Bala et al. 2010). Distinguishing them is important because their drivers emerge on different time scales, and thus the time scale of corresponding responses varies. This decomposition is typically assessed using a parallel set of idealized experiments in which aerosol emissions averaged over a particular time interval of interest are prescribed in both the fully coupled model and its atmosphere-only component (e.g., Samset et al. 2016; Liu et al. 2018).

While such a "time slice" approach serves as a valuable tool for studying the fundamental physical processes underlying the response to a fixed aerosol emission target, it becomes limited under transient conditions. Given the distinct spatial distributions and temporal evolutions of industrial and BMB aerosols, their varied aerosol types (primarily absorbing carbonous particles for BMB and predominantly scattering particles for industrial aerosols) and location-dependent efficacies (Persad and Caldeira 2018), it is crucial to account for their evolving trajectories when assessing their climate impacts. Under the transient framework, the separation between fast and slow responses becomes blurred. In particular, the response to time-evolving aerosol emissions in the absence of SST changes (e.g., the radiatively forced contribution) will include a slow component by virtue of the fact that aerosol emissions vary slowly through time. Thus, both the atmospheric radiative and ocean-mediated effects of aerosols must be considered on decadal and longer time scales. We emphasize that because aerosol forcing evolves slowly over time, the radiative response is not a purely fast adjustment in the classical sense.

To date, the climate response to time-evolving patterns of historical industrial and, to a lesser extent, BMB aerosol emissions has been investigated using fully coupled models (e.g., Deser et al. 2020; Wang and Wen 2022; Dong et al. 2024). While such studies highlight the importance of accounting for the full spatiotemporal evolution of aerosol emissions, they do not allow for insights into the relative contributions of atmospheric radiative versus ocean-mediated components of response. Moreover, the role of BMB aerosols and their interplay with industrial aerosols has been largely ignored.

We address these gaps by employing a novel atmospheric modeling framework to decompose the combined effects of time-varying industrial and BMB aerosol emissions into atmospheric radiative and ocean-mediated components. Specifically, we conduct a suite of experiments with Community Atmosphere Model, version 5 (CAM5), forced with time-varying historical aerosol (industrial plus BMB) emissions and associated SST responses individually and in combination, where the aerosol-induced SST changes are derived from the fully coupled Community Earth System Model, version 1 (CESM1), Single-Forcing and All-Forcing Large Ensembles (Kay et al. 2015; Deser et al. 2020). This approach allows us to elucidate the individual roles of evolving atmospheric radiative versus ocean-mediated impacts of industrial and BMB aerosols on historical climate change. A similar methodology has been previously used in the context of idealized 1% yr^{-1} CO_2 forcing (He and Soden 2015) and quadrupling of CO_2 concentration

Unauthenticated | Downloaded 10/07/26 05:58 PM UTC

TABLE 1. CAM5 AMIP experiments and their forcings. Each set of experiments contains 10 ensemble members and covers the period 1920–2030. See text for details.

	RAD-AMIP	SST-AMIP	FULL-AMIP
Radiative forcing	Time-varying industrial and BMB aerosol emissions. All other radiative forcings fixed at 1920 levels.	All radiative forcings fixed at 1920 levels.	Time-varying industrial and BMB aerosol emissions. All other radiative forcings fixed at 1920 levels.
SST/SIC forcing	SST and SIC fixed at 1920 levels.	Time-varying SST and SIC induced by industrial and BMB aerosol emissions.	Time-varying SST and SIC induced by industrial and BMB aerosol emissions.

(Shaw and Voigt 2015) experiments, but this is the first time it has been employed for the historical evolution of industrial and BMB aerosols to the best of our knowledge. If adopted in a model intercomparison effort, this framework could also be beneficial for understanding models' structural diversity in aerosol-induced climate change. In addition, this protocol may prove useful for informing dynamical and statistical regional downscaling applications, as it provides large-scale, aerosol-forced signals that can serve as consistent boundary conditions. This consistency is particularly valuable for intercomparisons across models and methods, where isolating the aerosol influence on regional climate remains a key challenge (Nabat et al. 2025).

This study has three aims: 1) to identify the dominant patterns of time-varying aerosol emissions from industrial and BMB sources over the historical period (1920–present); 2) to assess how the dominant patterns of time-evolving aerosol emissions influence precipitation, terrestrial air temperature, and the large-scale atmospheric circulation; and 3) to quantify the relative contributions of atmospheric radiative versus ocean-mediated pathways of response. We focus on boreal summer [June–August (JJA)], when NH monsoon systems and low-level jets drive strong signals, making it a natural season for assessing aerosol impacts particularly at regional scales. Our experimental design is described in section 2, results are reported in section 3, and summarized and discussed in section 4.

2. Data and methods

a. *Model simulations*

We use CAM5 (Neale et al. 2010) coupled to Community Land Model, version 4 (CLM4; Lawrence et al. 2011), at a spatial resolution of 1° for our AMIP simulations. CAM5 and CLM4 are the atmospheric and land model components of CESM1, respectively. CAM5 deploys a three-mode modal aerosol scheme (Liu et al. 2012) with prognostic aerosols and includes both the direct and indirect aerosol radiative effects for liquid and ice phase clouds (Morrison and Gettelman 2008). CLM4 includes a biogeochemical model which can prognostically simulate vegetation changes and a Snow and Ice Aerosol Radiation model which accounts for aerosol's impact on snow cover, as well as its radiative feedback.

At the time we conceived of this study, CESM1 was the only available version in the CESM family with both Single-Forcing and All-Forcing Large Ensembles, hence our choice of CAM5 for the AMIP experiments. Although CESM1 is an older framework, it remains scientifically robust and widely used. Further, it serves as an important benchmark for assessing the impact of horizontal resolution on simulated climate responses due to the advent of the new high-resolution (ocean eddy permitting) version of CESM1 and its 10-member All-Forcing Large Ensemble (Chang et al. 2026). CESM1 has a present-day aerosol effective radiative forcing of -1.37 W m^{-2} (Zelinka et al. 2014), which falls within the one standard deviation range of plausible estimates (Bellouin et al. 2020), and a transient climate response of 2.33°C, which falls within the very likely range of CMIP5 models (Meehl et al. 2013).

We conducted three sets of CAM5 AMIP ensembles, termed RAD-AMIP, SST-AMIP, and FULL-AMIP (Table 1). Each set has 10 ensemble members and covers the period 1920–2030. For each set, the ensemble members are initialized with a small (on the order of 10^{-14} K) random atmospheric temperature perturbation to create ensemble spread. RAD-AMIP uses time-varying CMIP5 historical (prior to 2006) and representative concentration pathway (RCP) 8.5 (2006 onward) industrial (AER_{indus}) and BMB (from agriculture activities, grass, and forest fires) aerosol emissions (Lamarque et al. 2010). All other radiative forcings, as well as SSTs and sea ice concentrations (SICs), are set to their 1920 ensemble-mean seasonal cycles from the 40-member CESM1 "All Forcing" Large Ensemble (ALL). SST-AMIP uses time-varying aerosol-induced SSTs and SICs; all radiative forcings including AER_{indus} and BMB are set to their 1920 ensemble-mean seasonal cycles in ALL. The time-varying aerosol-induced SSTs and SICs are computed from the difference between the ensemble mean of ALL and the sum of the ensemble means of the fixed AER_{indus} and fixed BMB CESM1 Single Forcing Large Ensembles following Deser et al. (2020). FULL-AMIP uses the same time-varying aerosol emissions as RAD-AMIP plus the same time-varying SSTs and SICs as SST-AMIP. In the following, we shall refer to the ensemble mean of the RAD-AMIP simulations as the "radiatively driven" or "atmospheric radiative" response and the ensemble mean of the SST-AMIP simulations as the "SST driven" or "ocean mediated" response.

We note that although RCP8.5 is an older radiative forcing scenario compared to the shared socioeconomic pathways (SSPs) used in CMIP6, it projects a more realistic evolution of post-2005 Asian aerosol emissions, with a peak during the 2010s followed by a decline through the 2020s and 2030s (Takemura 2012; Lund et al. 2019; IPCC 2021; Wang et al. 2024). In contrast, the SSP3-7.0 radiative forcing scenario

Unauthenticated | Downloaded 10/07/26 05:58 PM UTC

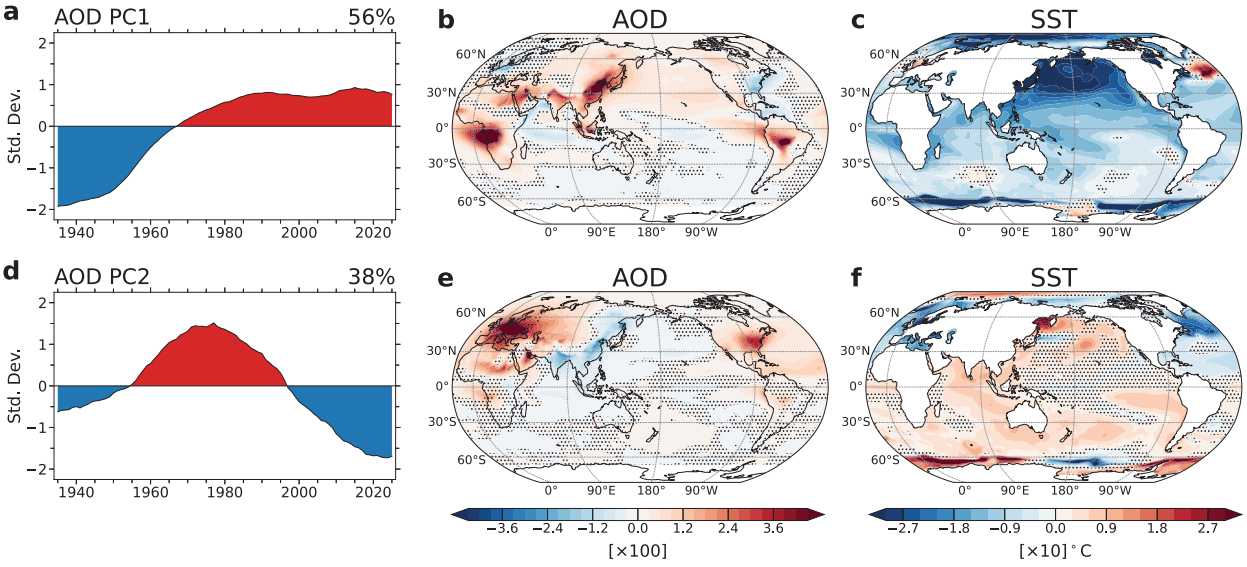


FIG. 1. (a),(d) PC time series of aerosol optical depth (AOD) in JJA based on FULL-AMIP. Percent variance explained by modes 1 and 2 (PC1 and PC2) is given in the upper right. Regression of JJA (b) AOD (×100) and (c) SST (°C ×10) in FULL-AMIP onto AOD PC1. (e),(f) As in (b) and (c), but for AOD PC2. Statistical significance of all regression values is assessed using a two-tailed Student's *t* test with effective degrees of freedom computed according to Bretherton et al. (1999) and applying the false discovery rate (FDR) with control level $\alpha_{FDR} = 0.05$ to measure the field significance of the response (Wilks 2016).

used for the CESM2 Large Ensemble (Rodgers et al. 2021) erroneously projects a continuous increase in China's aerosol emissions into the 2050s (Xiang et al. 2023). However, both scenarios fail to capture the observed AOD dipole between East and South Asia that has emerged since 2010 as a result of emissions reductions in China and simultaneous increases in India (Xiang et al. 2023).

b. *AOD and SST patterns*

To define the dominant patterns of aerosol radiative forcing in FULL-AMIP, we apply empirical orthogonal function (EOF) analysis to JJA AOD (550-nm wavelength) based on low-pass-filtered (using 10-yr running means) ensemble means from 1930 to 2030 (we exclude 1920–29 to minimize the influence of residual memory from ocean initial conditions). The two leading AOD modes account for 94% of AOD variance during 1930–2030 and are thus the focus of our analysis (nearly identical AOD modes are obtained from RAD-AMIP; Fig. S1 in the online supplemental material). To define the aerosol-induced SST patterns, we regress 10-yr low-pass-filtered ensemble mean SSTs in FULL-AMIP onto the normalized AOD principal component (PC) time series. The atmospheric responses to the two leading AOD modes are obtained by regressing 10-yr low-pass-filtered ensemble means of precipitation, sea level pressure (SLP), and land surface air temperature (LSAT) in FULL-AMIP, RAD-AMIP, and SST-AMIP onto the normalized AOD PCs. Using aerosol-induced SST PCs in place of AOD PCs yields similar atmospheric regression patterns (Figs. S2 and S3), despite the slight (3–4 year) phase lag between the SST PCs and AOD PCs (Fig. S4); thus, for simplicity, we use AOD PCs throughout this study. Statistical significance of all regression values is assessed using a two-tailed Student's *t* test at the 95% confidence level. Our results are not sensitive to the exact choice of running mean filter within the range 6–20 years, nor are they sensitive to the precise selection of start dates (1925–35) and end dates (2025–30). We emphasize that the AOD modes identified here should be viewed as diagnostic patterns characterizing the dominant spatiotemporal evolution of global industrial and biomass-burning aerosol emissions over the twentieth and early twenty-first centuries and may not necessarily represent dynamical modes.

3. Results

a. *Leading modes of AOD variability and associated SST patterns*

The two leading modes of JJA AOD variability show distinctive temporal and spatial characteristics (Fig. 1) and are statistically well separated according to the criterion of North et al. (1982). PC1, which explains 56% of the AOD variance, depicts a pronounced (three standard deviation) increase from the 1930s to the 1980s with little change thereafter, while PC2, which explains 38% of the AOD variance, shows more sinusoidal behavior, with a positive trend from about 1935 to 1975 followed by a steep decline to the early 2020s (Figs. 1a,d). The corresponding AOD spatial pattern associated with PC1 exhibits positive regression values over low latitudes of the Eastern Hemisphere, with regional hotspots in East and South Asia associated with industrial emissions and in tropical South Africa, South America, Indonesia, and Malaysia associated with BMB emissions; weak negative values are found in the eastern United States and western Europe (Fig. 1b). AOD mode 2 depicts a zonally asymmetric NH AOD pattern, with

Unauthenticated | Downloaded 10/07/26 05:58 PM UTC

large positive values in the eastern United States and western Europe juxtaposed against weaker negative values in South and East Asia from industrial aerosol emissions and in eastern Siberia from BMB emissions (Fig. 1e). The geographical breakdown of industrial and biomass burning aerosol contributions to the two AOD modes is shown in Fig. S5 based on CESM1.

The SST anomalies associated with AOD mode 1, obtained by regressing ensemble-mean JJA SST anomalies from FULL-AMIP onto AOD PC1, exhibit widespread cooling, as expected from the global increase in AOD (Fig. 1c). The cooling is greatest over the North Pacific and along the sea ice margins of both hemispheres. A strong interhemispheric SST anomaly gradient is evident over the Pacific sector and, to a lesser extent, the Indian Ocean, likely associated with aerosol emissions over South and East Asia (Hwang et al. 2024). Pronounced SST warming is found in the central subpolar North Atlantic. This may be associated with a strengthening of AMOC and accompanying increase in northward ocean heat transport in response to AOD reductions over eastern North America and Europe (Cai et al. 2006; Delworth and Dixon 2006; Booth et al. 2012; Menary et al. 2020; Dagan et al. 2020), but local wind-driven processes may also play a role.

The SST anomalies associated with AOD mode 2 are generally weaker than those associated with mode 1 and depict a strong zonal contrast over the NH with widespread cooling over the North Atlantic and Mediterranean and warming over most of the North Pacific (Fig. 1f). The North Atlantic cooling likely arises in response to increased aerosol emissions over the eastern United States and Europe (e.g., Undorf et al. 2018a), while the warming in the Pacific and Indian Ocean sectors is presumably a result of reduced AOD over eastern Asia and India (Fig. 1f).

Investigation of the mechanisms underlying the SST patterns associated with each AOD mode is beyond the scope of this study, but related analyses may be found in Kang et al. (2021), Shi et al. (2022), Hwang et al. (2024), and Diao et al. (2025), although none considered the combined effects of industrial and BMB aerosols. Here, our interest is in how these aerosol-induced SST patterns impact the atmosphere.

b. *Global atmospheric response patterns*

We begin by examining the global atmospheric response to combined atmospheric radiative and SST-driven changes associated with each AOD mode. To do this, we regress the FULL-AMIP JJA ensemble means onto the PC time series associated with each AOD mode. Regression maps of precipitation, SLP, and LSAT for AOD mode 1 are shown in Fig. 2 and for AOD mode 2 in Fig. 3. Regression maps for associated short-wave surface downward (SWSD) radiative flux under total-sky, clear-sky, and cloudy-sky conditions in both modes are given in Fig. 4.

Both modes exhibit statistically significant responses that are global in scale. AOD mode 1 features prominent drying over South and East Asia, the northern Indian Ocean, and the Maritime Continent, regions proximate to the main centers of AOD increase (Fig. 2a), accompanied by reduction in SWSD (Fig. 4a). Compensating areas of wetting occur directly south of the equator in the Indian Ocean and central Pacific. At higher latitudes, widespread drying is found over the Southern Ocean, the North Pacific, northeastern Asia, and western North America, while wetting occurs over the subtropical south Indian and southeast Pacific Oceans, tropical Africa, southern Europe, the Caribbean, and parts of the North Atlantic. Areas of drying (wetting) generally correspond to anticyclonic (cyclonic) SLP anomalies, with largest SLP magnitudes in the extratropics (Fig. 2d). The prominent positive SLP response over the North Pacific may be due to in part to a remote Rossby wave teleconnection excited by precipitation reductions over the northern Indian Ocean and Southeast Asia (Smith et al. 2016; Dittus et al. 2021) in addition to local SST cooling. Additional detail on the circulation responses over the tropical Indo-Pacific and Southern Hemisphere high latitudes is provided in section 3c. AOD mode 1 exhibits widespread terrestrial cooling (Fig. 2g), as expected from the global-scale increase in AOD (Figs. 1a,b) with widespread SWSD reductions (Fig. 4a). The strongest cooling is found in boreal regions, likely associated with positive ice/snow albedo feedback. A "cooling hole" is seen over far western Europe, reflecting the local decrease in AOD with positive SWSD values (Fig. 4a). SWSD in FULL-AMIP closely resembles that in RAD-AMIP, whereas SST-driven SWSD responses primarily associated with cloud changes are much weaker. Cloud responses to aerosol strongly affect the SWSD response in remote regions (Fig. 4e), whereas the direct radiative effect dominates locally (Fig. 4c).

AOD mode 2 shows generally weaker responses compared to mode 1, especially for precipitation and LSAT (Fig. 3). Like mode 1, mode 2 AOD increases are generally accompanied by local terrestrial drying and cooling (Figs. 1e and 3g). For example, AOD increases over Europe and the eastern United States are accompanied by negative SWSD, primarily driven by aerosol–cloud interactions, whereas AOD decreases over eastern Asia and India produce the opposite response (Figs. 4b,f,h). Remote precipitation responses are also evident, most prominently in the tropics, including a zonal dipole pattern of drying over the far western Pacific and wetting over the central Indian Ocean and an increase in precipitation across the equatorial Atlantic. The large-scale SLP response over the extratropical NH is generally opposite in sign between modes 1 and 2, in keeping with their contrasting NH AOD signatures (Figs. 2d, 3d and 4a,b). However, the tropical and SH SLP response patterns are distinctive between the two AOD modes.

Next, we assess the relative contributions of atmospheric radiative and ocean-mediated pathways to the atmospheric responses in FULL-AMIP by regressing ensemble-mean fields from RAD-AMIP and SST-AMIP onto the AOD PCs derived from FULL-AMIP. The two pathways produce distinctive and statistically significant global-scale atmospheric responses (Figs. 2 and 3). Comparing to FULL-AMIP, it is readily apparent that the SST-driven response dominates the large-scale patterns of precipitation and SLP response, while radiative forcing tends to oppose SST-induced responses, although the degree of compensation varies with region. On the other hand, radiatively forced and SST-driven responses make comparable contributions to the LSAT response in FULL-AMIP. Quantitatively, the leading role

Unauthenticated | Downloaded 10/07/26 05:58 PM UTC

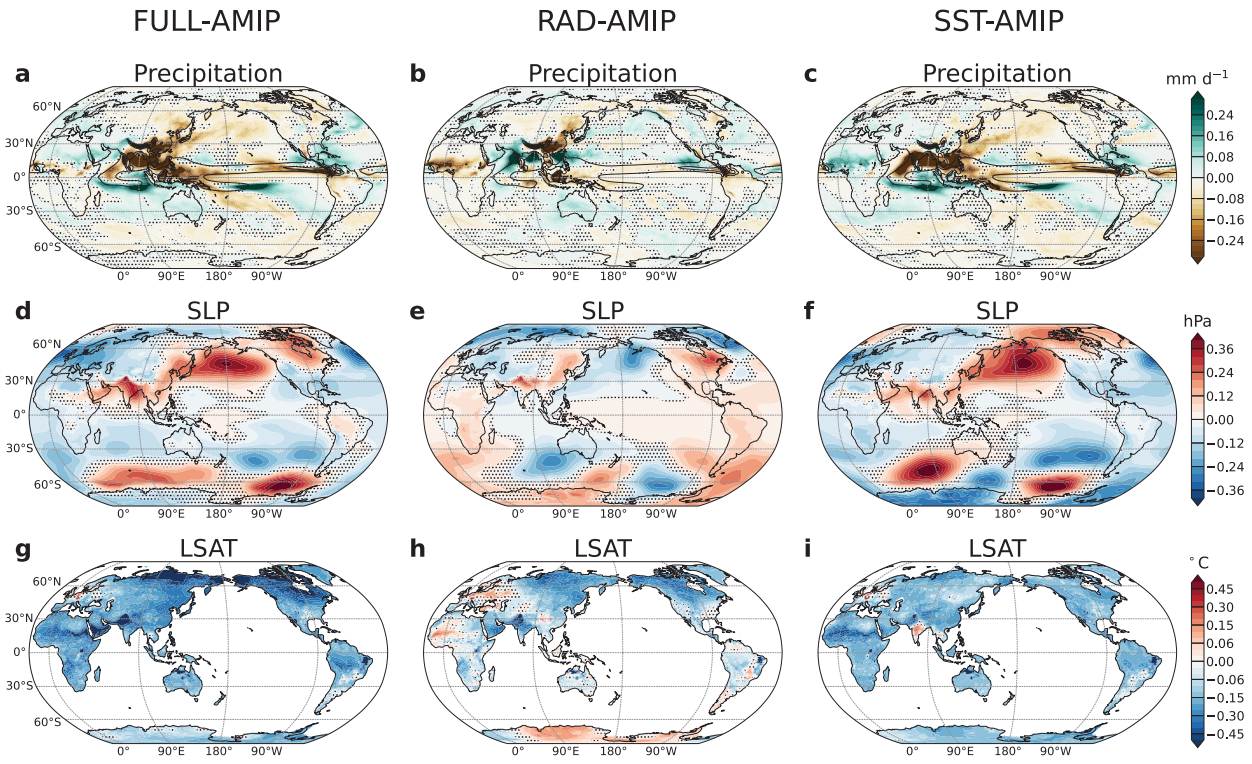


FIG. 2. Regressions onto FULL-AMIP AOD PC1 for (a)–(c) precipitation (mm day^{-1}), (d)–(f) SLP (hPa), and (g)–(i) LSAT (°C) in FULL-AMIP, RAD-AMIP, and SST-AMIP. Statistical significance of all regression values is assessed using a two-tailed Student's t test with effective degrees of freedom computed according to Bretherton et al. (1999) and applying the false discovery rate (FDR) with control level $\alpha_{FDR} = 0.05$ to measure the field significance of the response (Wilks 2016).

of the SST-induced response for the precipitation and SLP responses is evidenced by the high pattern correlations (exceeding 0.70) between SST-AMIP and FULL-AMIP, while those between RAD-AMIP and FULL-AMIP are substantially lower (<0.33; Fig. 5). In contrast, the importance of both radiative forcing and ocean-mediated effect to the patterns of LSAT response is reflected in the comparable magnitudes of spatial correlation between RAD-AMIP and FULL-AMIP and between SST-AMIP and FULL-AMIP (around 0.65 and around 0.75, respectively; Fig. 5). Radiative forcing partially counteracts the SST-driven response for both precipitation and SLP responses, as seen by the modest negative pattern correlations between RAD-AMIP and SST-AMIP (Fig. 5). This negative correlation is particularly pronounced for the SLP response to AOD mode 1 (−0.60), as is also visually apparent (Figs. 2e,f). However, for LSAT, the correlations between RAD-AMIP and SST-AMIP are weakly positive (Fig. 5).

As mentioned above, the interplay between atmospheric radiative and ocean-mediated pathways depends on the region and quantity of interest. In emission source regions such as East Asia, precipitation responses in both AOD modes are primarily driven by radiative forcing: In mode 1, AOD increases induce local drying, while AOD decreases in mode 2 induce local wetting (Figs. 1a,d, 2b and 3b). In contrast, the sign of South Asian precipitation response does not always align with local AOD changes because the SST-driven response dominates. For example, in AOD mode 1, radiative forcing drives a wetting response despite positive AOD values over South Asia, and this radiatively forced wetting is largely offset by SST-driven drying (Figs. 1a and 2b,c). In the NH midlatitudes, eastern North America and Europe exhibit robust precipitation and LSAT responses to both AOD modes, driven by a combination of radiatively induced and SST-driven thermodynamic and dynamic mechanisms (Figs. 2b,c and 3b,c). In these regions, LSAT changes reflect compensation between radiatively forced and SST-driven responses, whereas western European precipitation results from the reinforcement of the two pathways of response. Over North America, radiatively and SST-driven precipitation and LSAT responses exhibit distinct patterns, reflecting a tug-of-war between locally and remotely induced circulation influences. For example, in AOD mode 1, radiative forcing drives a positive North Atlantic Oscillation (NAO)-like response and a slight intensification of the Aleutian low, while SST forcing drives a negative NAO-like response and a marked weakening of the Aleutian low (Figs. 2e,f). Whether these large-scale circulation responses are triggered by local or remote forcing is hard to determine, warranting further analysis.

In low-emission regions, such as the Sahel, radiatively forced and SST-driven precipitation responses cancel each other, resulting in a muted overall response for both AOD modes (Figs. 2b,c and 3b,c). In contrast, radiatively induced and ocean-mediated SLP responses for mode 2 are of the same sign over most of the

Unauthenticated | Downloaded 10/07/26 05:58 PM UTC

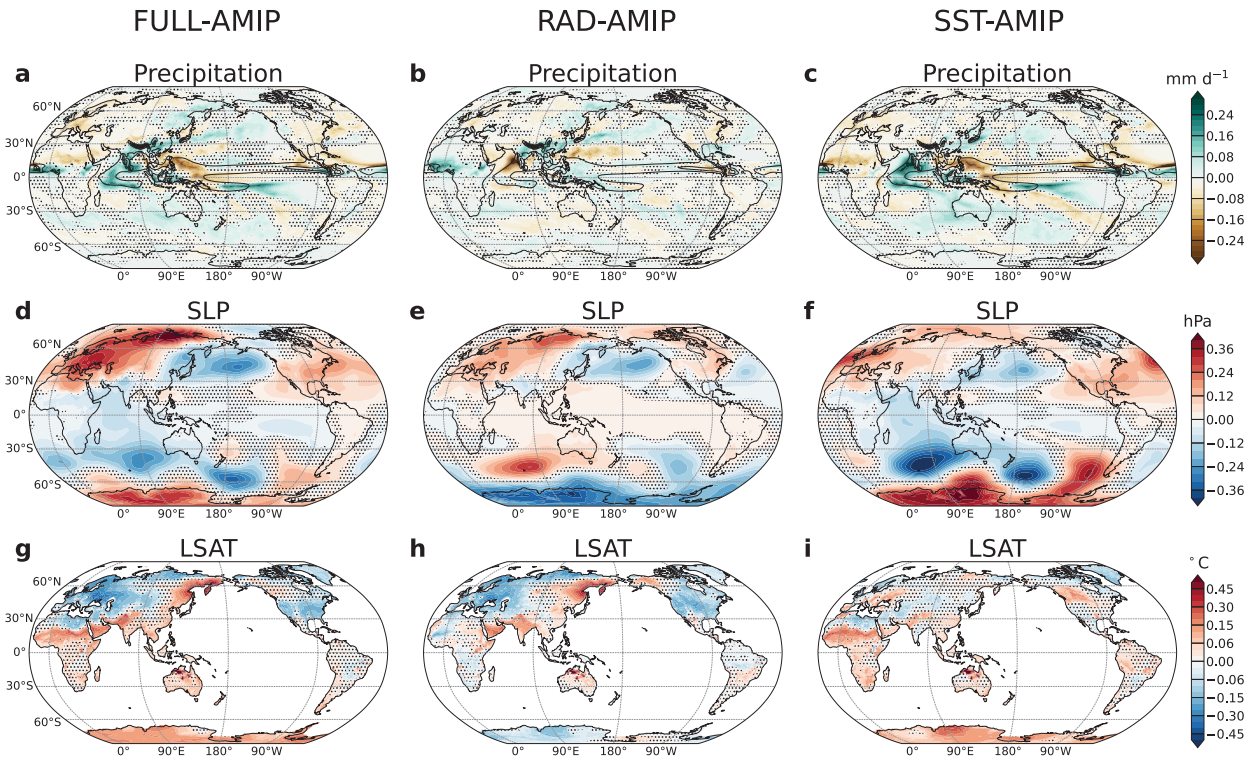


FIG. 3. As in Fig. 2, but for AOD PC2.

NH and tropics but of opposite polarity over the SH high latitudes (Figs. 3e,f). The NH LSAT response to AOD mode 1 shows like-signed contributions from radiatively forced and SST-driven responses (Figs. 2h,i), whereas the LSAT response to AOD mode 2 depicts nearly orthogonal patterns (Figs. 3h,i).

The complex regional interplay between radiatively forced and SST-driven responses raises the question: To what extent are these responses additive? We address this by comparing the FULL-AMIP regressions with the sum of the RAD-AMIP and SST-AMIP regressions (SUM) in Fig. 6 for mode 1 and Fig. S6 for mode 2. Both AOD modes show a large degree of additivity, as evidenced by the overall similarity in pattern and amplitude between SUM and FULL-AMIP. In general, the differences between SUM and FULL-AMIP are relatively small in magnitude, albeit statistically significant, except for SLP at high latitudes where larger discrepancies are found. Pattern correlations between SUM and FULL-AMIP are high (0.79–0.92) for all three variables in both AOD modes (Fig. 5).

A separate but related question is to what extent does the FULL-AMIP response resemble the fully coupled CESM1 response to industrial and BMB aerosol emissions? Since AMIP simulations necessarily exclude coupled ocean–atmosphere feedbacks by virtue of their design, it is not a given that the response in FULL-AMIP matches that of CESM1 (AER_{indus} + BMB). Figure 7 compares the regression maps based on FULL-AMIP with those based on CESM1 (AER_{indus} + BMB) for AOD mode 1; results for mode 2 are shown in Fig. S7. The precipitation responses are generally similar between the two model configurations (global pattern correlation of 0.86; Fig. 5), with slightly reduced magnitudes in CESM1 compared to FULL-AMIP, particularly over the tropical Indian Ocean and South Asian sector (Figs. 7a,b). In this sector, their difference (CESM1 minus FULL-AMIP) closely resembles the ocean-mediated response pattern but with opposite sign (recall Fig. 2c), indicating that the response in FULL-AMIP (and SST-AMIP) is slightly overestimated due to the lack of air–sea feedbacks. Analogous results are found for the precipitation response to AOD mode 2 (cf. Fig. S7c with Fig. 3c). The SLP responses for AOD mode 1 show relatively minor differences between CESM1 and FULL-AMIP over the extratropical NH, but considerable discrepancies in magnitude are found over the extratropical SH (Figs. 7d–f), which lower the overall global pattern correlation to 0.56 (Fig. 5). These high-latitude circulation disparities may indicate a role for air–sea feedbacks (damping the response over the Pacific and enhancing it over the Indian Ocean: compare with the ocean-mediated response in Fig. 2f), and/or they may stem from the high levels of intrinsic atmospheric variability in austral winter that are not sufficiently eliminated with 10-member ensembles (although our statistical significance test would seem to refute this possibility). Analogous results are found for AOD mode 2 (Figs. S7d–f). Finally, the LSAT responses for AOD mode 1 are generally similar between the two model configurations (global pattern correlation of 0.74; Fig. 5), with a slight overestimate of the cooling in FULL-AMIP compared to CESM1 (except over Antarctica and western Canada), which may be due to neglected damping

Unauthenticated | Downloaded 10/07/26 05:58 PM UTC

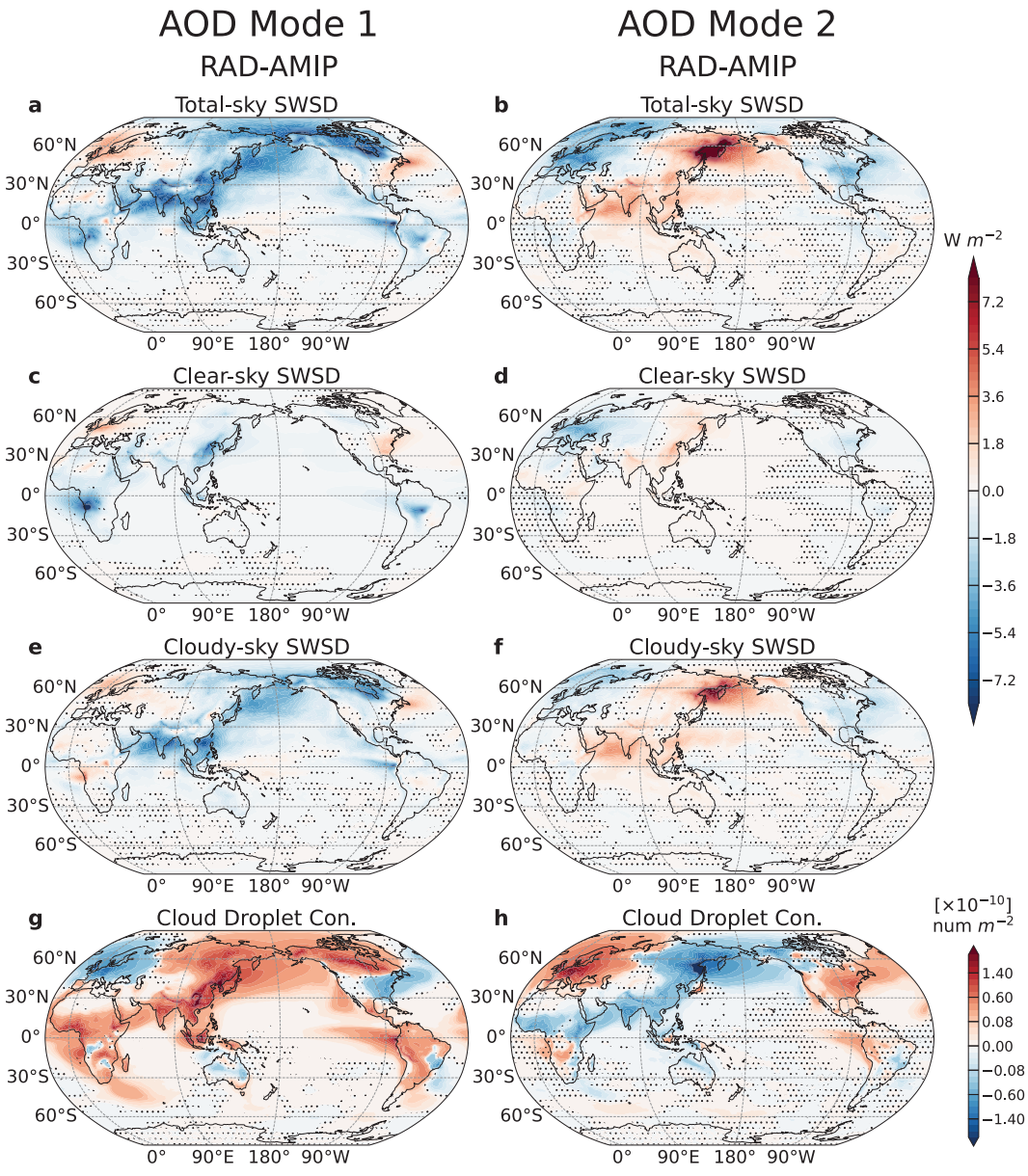


FIG. 4. Regressions onto FULL-AMIP AOD PC1 and PC2 for SWSD radiative flux (W m^{-2}) under (a),(b) total-sky, (c),(d) clear-sky, and (e),(f) cloudy-sky conditions, and for (g),(h) vertically integrated cloud droplet number concentration (num $m^{-2} \times 10^{-10}$) in RAD-AMIP. Statistical significance of all regression values is assessed using a two-tailed Student's t test with effective degrees of freedom computed according to Bretherton et al. (1999) and applying the false discovery rate (FDR) with control level $\alpha_{FDR} = 0.05$ to measure the field significance of the response (Wilks 2016).

feedbacks from land–atmosphere coupling (Figs. 7g–i). The LSAT responses to AOD mode 2 show only minor discrepancies between the two model configurations (Figs. S7g–i). In summary, despite the lack of air–sea coupling in the FULL-AMIP protocol, the atmospheric responses to both AOD modes are largely similar to those of CESM1 with exceptions as noted above. This lends confidence to the utility of our AMIP approach for dissecting the fully coupled model's response to time-evolving aerosol emissions.

c. *Regional atmospheric response patterns*

The diversity of regional features described above makes it difficult to generalize the relative contributions of atmospheric radiative versus ocean-mediated pathways on aerosol-driven atmospheric responses at the regional scale. To further illustrate this regional variation, we focus here on two areas: the tropical Indo-Pacific sector and Southern Ocean, characterized by distinct response patterns, to demonstrate how radiative forcing originating from regional AOD changes

Unauthenticated | Downloaded 10/07/26 05:58 PM UTC

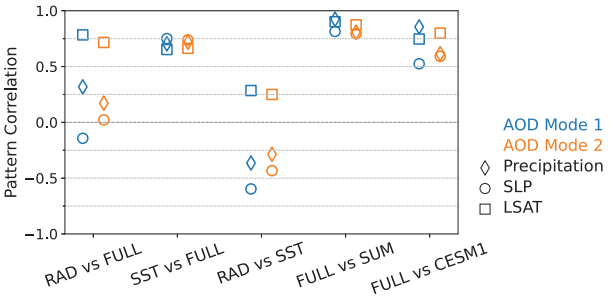


FIG. 5. Global pattern correlations of precipitation (diamond), SLP (circle), and LSAT (square) regression maps associated with AOD mode 1 (blue) and AOD mode 2 (orange) between different pairs of AMIP simulations. RAD refers to RAD-AMIP, SST refers to SST-AMIP, SUM refers to the sum of RAD-AMIP and SST-AMIP regressions, and FULL refers to FULL-AMIP. Also included are the global pattern correlations between the fully coupled CESM1 and FULL-AMIP (see text for details).

interacts with the SST-driven response to influence the atmosphere locally and remotely.

1) TROPICAL INDIAN–WESTERN PACIFIC SECTOR

The pattern of precipitation response to AOD mode 1 features a distinctive meridional dipole over the tropical Indian–western Pacific sector in FULL-AMIP (Fig. 8a), indicative of an Asian summer monsoon response to shifting historical aerosol emissions that has been a topic of great interest in the literature (Bollasina et al. 2011; Persad et al. 2017; Undorf et al. 2018b; Westervelt et al. 2020). In our simulations, this precipitation dipole response corresponds to a cross-equatorial overturning circulation, with northerly wind anomalies at low levels and southerly wind anomalies at upper levels, which feeds anomalous upward motion along 5°–10°S accompanied by anomalous downward motion along 5°–15°N (Figs. 8a,b). This cross-equatorial overturning circulation response results from a subtle interplay between radiatively forced and SST-driven responses, which impart different meridional scales and polarities of response. The radiatively forced response exhibits a narrow meridional dipole between the Asian subcontinent from the Tibetan Plateau eastward (27°–30°N) and the northern Indian Ocean–western Pacific (14°–23°N; Figs. 8c,d), while the SST-driven response displays a broader latitudinal dipole structure between the northern (5°–20°N) and southern (5°–12°S) portions of the Indian Ocean (Figs. 8e,f). The radiatively forced and SST-driven responses are offsetting over the northern Indian Ocean. As a result, the response in FULL-AMIP shows a hybrid structure, with characteristics of both the SST-driven response (i.e., the broad cross-equatorial dipole, albeit substantially weaker in its northern lobe) and the radiatively forced response (i.e., the narrow meridional dipole over the Tibetan Plateau extending eastward).

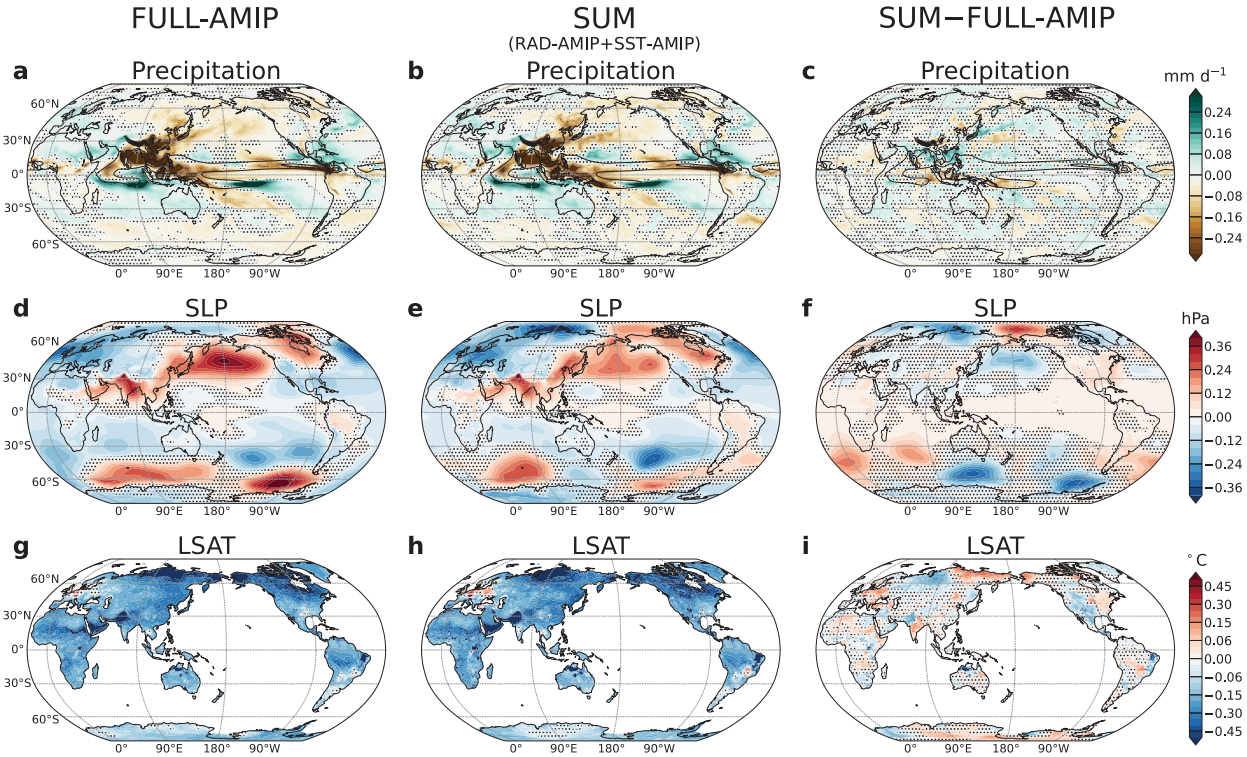


FIG. 6. As in Fig. 2, but for additivity analysis based on AOD mode 1. (a),(d),(g) FULL-AMIP, (b),(e),(h) the sum of RAD-AMIP and SST-AMIP (SUM), and (c),(f),(i) the difference between SUM and FULL-AMIP. Statistical significance of all regression values is assessed using a two-tailed Student's t test with effective degrees of freedom computed according to Bretherton et al. (1999) and applying the false discovery rate (FDR) with control level $\alpha_{FDR} = 0.05$ to measure the field significance of the response (Wilks 2016). Black contours on precipitation panels show the climatological 6 mm day^{-1} isopleth.

Unauthenticated | Downloaded 10/07/26 05:58 PM UTC

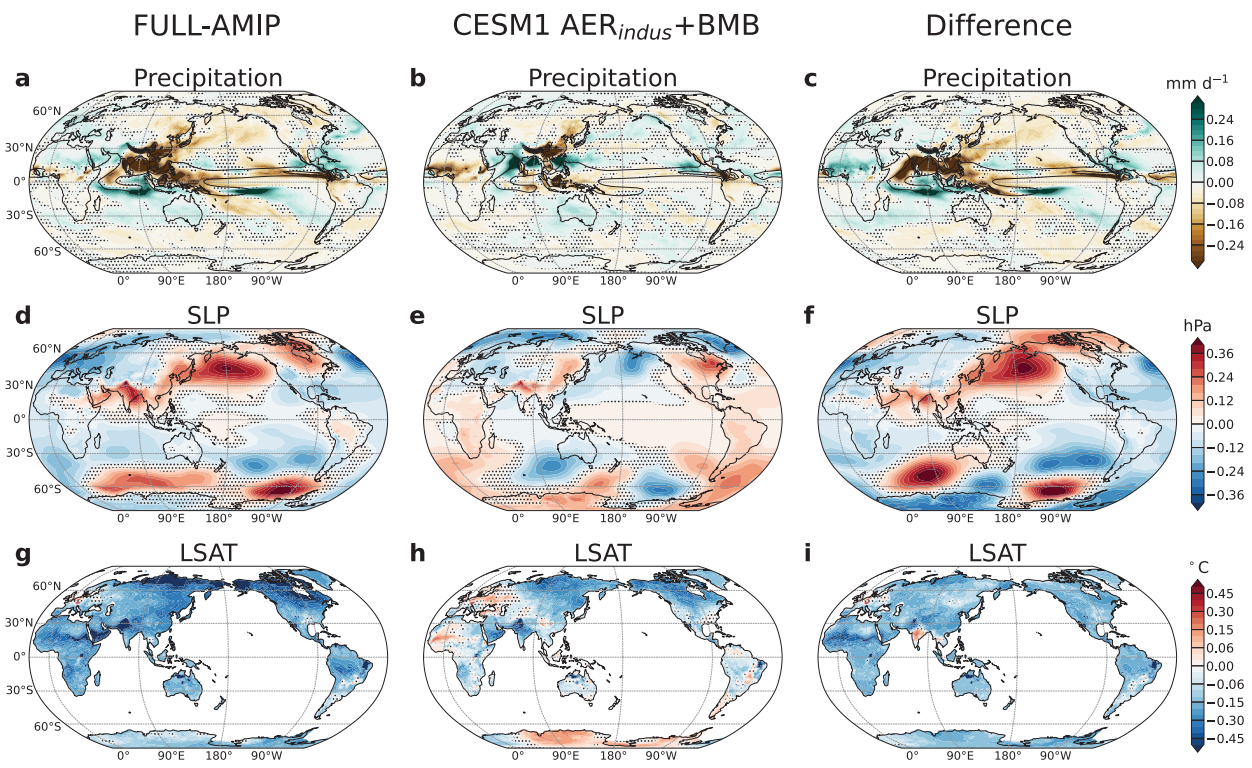


FIG. 7. Regressions of precipitation, SLP, and LSAT in (left) FULL-AMIP and (center) CESM1-AER$_{\text{indus}}$ + BMB, and (right) their difference (CESM1 minus FULL-AMIP) based on AOD PC1 from FULL-AMIP. Statistical significance of all regression values is assessed using a two-tailed Student's t test with effective degrees of freedom computed according to Bretherton et al. (1999) and applying the false discovery rate (FDR) with control level $\alpha_{\text{FDR}} = 0.05$ to measure the field significance of the response (Wilks 2016).

The SST-driven precipitation dipole response (Figs. 2a and 8a) likely results from the enhanced meridional temperature gradient over the Indian Ocean (i.e., stronger cooling north of the equator than south; Li et al. 2020), although the pronounced large-scale cooling of the North Pacific may also play a role in displacing the rain belt southward (recall Fig. 1c). Conversely, the radiatively forced precipitation dipole response is likely driven by locally induced drying and subsidence from aerosol emissions over East Asia, with compensating upward motion over the Arabian Sea, Bay of Bengal, and South China Sea (Bollasina et al. 2011; Persad et al. 2017; Westervelt et al. 2020); enhanced cooling over land may also contribute to ascent over the nearby seas.

Both aerosol direct and indirect radiative effects contribute to enhanced cooling over Southeast Asia in RAD-AMIP, as seen from the SWSD under clear and cloudy skies, respectively (Figs. 4a,c,e). Aerosol direct effects (e.g., clear-sky SWSD) dominate locally over the aerosol emission source regions (Fig. 4c), while aerosol indirect effects (e.g., cloudy-sky SWSD and associated increase in cloud droplet number concentration) prevail in adjacent regions including the northern Indian Ocean (Figs. 4e,g). Note that the reduction in cloudy-sky SWSD over the northern Indian Ocean and western North Pacific in RAD-AMIP would act to cool the underlying SSTs if the ocean were allowed to respond, consistent with the negative SST anomalies found in SST-AMIP. In SST-AMIP, adiabatic heating associated with the descending branch of the overturning circulation response over the northern Indian Ocean (Figs. 8e,f) reduces cloud cover and allows more insolation to reach the surface (not shown), warming the adjacent Indian Peninsula and parts of central mainland Southeast Asia (Fig. 2i). However, this warming effect is overwhelmed by radiatively forced cooling (Fig. 2h), resulting in net cooling over these regions in FULL-AMIP (Fig. 2g).

The relative role of RAD-AMIP (i.e., atmosphere radiative effects) versus SST-AMIP (i.e., ocean-mediated effects) provides valuable insight on the relative importance of in situ versus large-scale responses to aerosol changes in driving summertime rainfall trends in this region, which has been a topic of substantial debate (Bollasina et al. 2011; Persad et al. 2017; Dong et al. 2019; Li et al. 2018; Wang et al. 2019; Westervelt et al. 2020). AOD mode 1 captures prevailing northerly wind anomalies and precipitation reductions over Asian summer monsoon land regions, indicating a weakening of Asian summer monsoon (Li et al. 2018; Wang et al. 2019). The SST-driven cross-equatorial dipole circulation accounts for the precipitation response over the central to southern Indian Peninsula and adjacent oceans. In contrast, East Asian monsoon weakening arises primarily from a local, radiatively dominated response, with subsiding motion accompanied by terrestrial cooling and positive SLP anomalies, that in turn suppresses ascending motion over the Tibetan

Unauthenticated | Downloaded 10/07/26 05:58 PM UTC

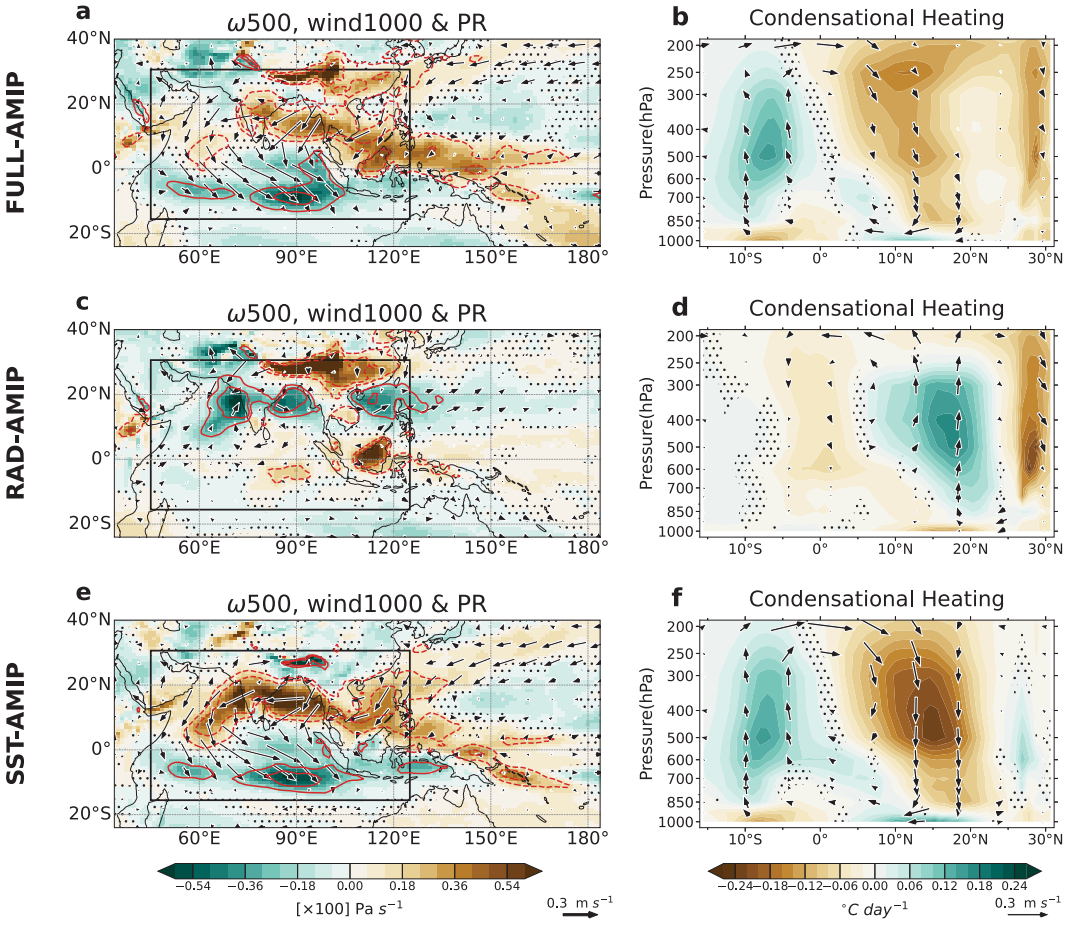


FIG. 8. AOD mode 1 tropical Indo-Pacific response of (a),(c),(e) 500-hPa ω (Pa s^{-1} × 100; color shading), 1000-hPa vector wind (m s^{-1}; reference vector in lower right), and precipitation (mm day^{-1}; red contours), and (b),(d),(f) zonally averaged (45°–125°E) condensational heating (°C day^{-1}; color shading) and v, ω vectors (v: m s^{-1}; reference vector in lower right; ω: Pa s^{-1} × 50) in FULL-AMIP, RAD-AMIP, and SST-AMIP regressed onto AOD PC1. Red contours in (a), (c), and (e) show precipitation regression slopes, starting from ±0.2 mm day^{-1} and contoured at ±0.2 mm day^{-1} intervals, with solid lines for positive values and dashed lines for negative values. Statistical significance of all regression values is assessed using a two-tailed Student's t test with effective degrees of freedom computed according to Bretherton et al. (1999) and applying the false discovery rate (FDR) with control level $\alpha_{FDR} = 0.05$ to measure the field significance of the response (Wilks 2016). Horizontal wind magnitudes < 0.01 m s^{-1} are omitted for clarity.

Plateau extending eastward. These results suggest that historical South Asian summer monsoon weakening reflects effects of East Asian aerosols (Shawki et al. 2018) in mode 1 here, given the importance of the ocean-mediated response. But when not decomposed by mode, the full response of South Asian summer monsoon to aerosols likely includes contributions from other remote sources such as Europe and North America (Bollasina et al. 2014; Undorf et al. 2018b). In contrast, East Asian monsoon weakening is primarily attributable to local aerosols through the atmospheric radiative pathway. Given that the total response of East Asian summer monsoon precipitation to aerosols is dominated by mode 1 and partially compensated by mode 2, in keeping with their opposite-signed local AOD anomalies (Figs. 1b,d, 2a, and 3a), this indicates that historical East Asian summer monsoon weakening and associated land drying are likely dominated by local aerosols through the atmospheric radiative pathway.

2) SOUTHERN HEMISPHERE CIRCULATION

A notable aspect of AOD mode 1 is the SLP response pattern over the SH, which resembles a Rossby wave train in both RAD-AMIP and SST-AMIP but with opposite signs (Figs. 2e,f). In contrast, FULL-AMIP shows a zonally symmetric structure over the SH extratropics, with positive (negative) SLP anomalies at high (mid-) latitudes (Fig. 2d). SH circulation trends have been linked to anomalous heating in the tropics which can trigger tropical–extratropical teleconnections (Berbery et al. 1992; Hoskins and Ambrizzi 1993). Guided by this theory, we pose an open question: Can low-latitude

Unauthenticated | Downloaded 10/07/26 05:58 PM UTC

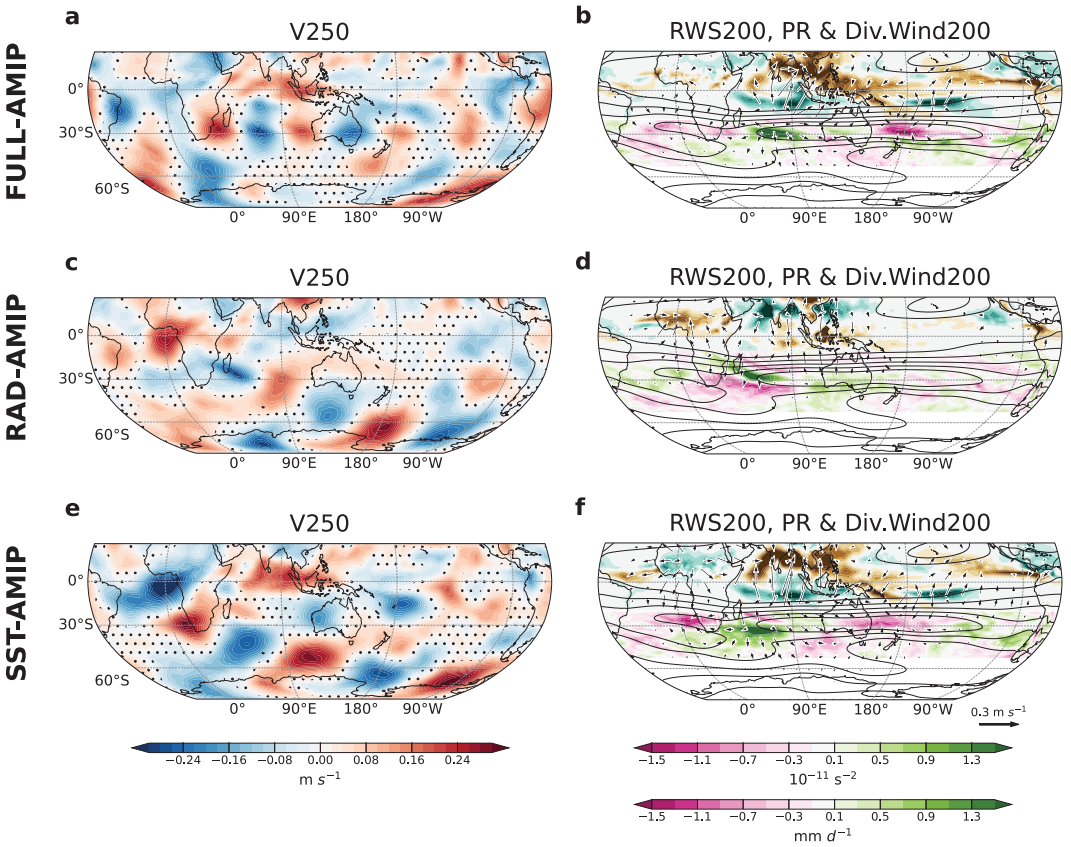


FIG. 9. AOD mode 1 Southern Hemisphere response of (a),(c),(e) 250-hPa meridional wind (V250; m s^{-1}) and (b),(d),(f) 200-hPa RWS (RWS200; pink–green color bar; 10^{-11} s^{-2}), precipitation (PR; green–brown color bar; mm day^{-1}), and 200-hPa divergent wind vector (m s^{-1}; reference vector in lower right) regressed onto AOD PC1 in FULL-AMIP, RAD-AMIP, and SST-AMIP. For clarity, RWS200 (precipitation) regressions are only shown in the latitude band 52°–20°S (19°S–26°N) in FULL-AMIP and SST-AMIP and 52°–6°S (6°S–26°N) in RAD-AMIP; wind vectors with magnitudes < 0.03 m s^{-1} are omitted. The climatological 250-hPa zonal wind is contoured in black (contour interval = 10 m s^{-1} from 5 to 45 m s^{-1}). Statistical significance of all regression values is assessed using a two-tailed Student's t test with effective degrees of freedom computed according to Bretherton et al. (1999) and applying the false discovery rate (FDR) with control level $\alpha_{FDR} = 0.05$ to measure the field significance of the response (Wilks 2016).

aerosols, particularly central African BMB emissions given their geographic proximity, modulate SH circulation through teleconnection dynamics via an atmospheric radiative pathway, and how does this compare with teleconnections driven by the ocean-mediated response? These SH anomalous upper-level circulations can potentially influence Australian precipitation (Ashok et al. 2003; Cai et al. 2011) and Antarctic climate through the tropical–Antarctic teleconnection (Ding and Steig 2013; Li et al. 2021).

To understand the origin of the Rossby wave train responses, we examine the upper-level circulation and its connection to tropical precipitation. The 250-hPa meridional wind (V250) anomalies clearly delineate poleward-propagating Rossby wave trains of opposite sign in response to the radiatively forced and SST-driven responses, which appear to originate in the Gulf of Guinea and propagate southeastward over the southern Indian Ocean and into the Pacific sector of the Southern Ocean (Figs. 9c,e). The SST-driven Rossby wave train takes a slightly more poleward route than the radiatively forced one. FULL-AMIP lacks a poleward-propagating Rossby wave signature due to the large degree of cancellation between RAD-AMIP and SST-AMIP (Fig. 8a). Instead, FULL-AMIP shows a zonally oriented V250 wave train emanating from the tip of South Africa and extending eastward across the Indian and Pacific Oceans along the latitude (30°S) of the subtropical jet maximum, which acts as a waveguide (Fig. 9b).

Both the radiatively forced and SST-driven V250 Rossby wave trains appear to be initiated by tropical precipitation and associated diabatic heating anomalies over Africa and the Indian Ocean (Figs. 9d,f). In SST-AMIP, upper-level divergence associated with increased precipitation over the Sahel produces the negative (northerly) V250 anomaly centered over the Gulf of Guinea (Fig. 9f). As the anomalous northerly divergent winds cross the equatorward flank of the climatological subtropical westerly jet, they generate a negative Rossby wave source (RWS) to the west of South Africa,

Unauthenticated | Downloaded 10/07/26 05:58 PM UTC

which triggers a downstream Rossby wave response (Fig. 9f). Increased precipitation in the tropical Indian Ocean along 10°S may also act to reinforce the Rossby wave response. These results are consistent with previous studies which show the critical role of the subtropical jet in amplifying upper-level circulation anomalies emanating from tropical heating (Berbery et al. 1992; Hoskins and Ambrizzi 1993; Li et al. 2015) and serving as a waveguide into the SH extratropics (Gillett et al. 2022). In RAD-AMIP, upper-level convergence associated with diminished precipitation over the Sahel produces the positive (southerly) V250 anomaly centered over the Gulf of Guinea (Fig. 9d). Unlike SST-AMIP, however, RAD-AMIP shows a large AOD increase over the African Democratic Republic associated with local BMB emissions (recall Fig. 1b). The resulting anomalous heat source from absorbing BMB aerosols is balanced by adiabatic ascent, accompanied by upper-level divergence (Fig. 9d). The divergent V250 anomaly crossing the equatorward flank of the subtropical jet over the southwestern Indian Ocean generates a positive RWS anomaly, which in turn triggers the downstream Rossby wave train response (Fig. 9d). We emphasize that the mechanistic explanations offered above remain speculative and warrant further investigation using targeted experiments with simpler (e.g., linear barotropic) models forced with regional heating and vorticity anomalies.

4. Summary and discussion

There is increasing recognition that the global climate response to anthropogenic aerosols is sensitive to the pattern of regional emissions, which has shifted over time, necessitating a broader view of their role in historical climate change (Persad and Caldeira 2018; Deser et al. 2020; Kang et al. 2021; Wang and Wen 2022; Persad 2023; Shi et al. 2022; Dong et al. 2024; Diao et al. 2025). In particular, two distinct modes of AOD variability from industrial sources have been identified over the past century: the "global increase mode" primarily associated with Asian emissions but modulated by emissions over North America and Europe, and the "shift mode" reflecting a zonal redistribution of NH emissions between the Western and Eastern Hemispheres (Kang et al. 2021; Wang and Wen 2022; Shi et al. 2022; Dong et al. 2024). These AOD modes can produce synergistic and competing effects with greenhouse gases (GHGs) depending on the period of interest, complicating detection and attribution efforts (Dong et al. 2024). The dynamical mechanisms underpinning the global response to the "global increase" and "shift" modes of industrial aerosol emissions have been investigated in idealized coupled modeling studies, revealing the importance of both atmospheric and oceanic processes (Kang et al. 2021; Wang and Wen 2022; Shi et al. 2022; Diao et al. 2025). However, nonlinear interactions between aerosol emissions in different regions complicate a full understanding and interpretation of the combined effects of the two AOD modes (Diao et al. 2025).

In this study, we provide additional insight into the pathways by which time-evolving anthropogenic aerosols from combined industrial and BMB sources over the past century influence boreal summer (JJA) climate. In particular, we utilize a novel atmospheric modeling framework based on CESM1 (CAM5) to separate the atmospheric radiative and ocean-mediated pathways of response. We partition the full spatiotemporal evolution of historical aerosol emissions into two leading diagnostic patterns based on EOF analysis and elucidate the response pathways for each.

AOD variations arising from industrial and BMB sources can be decomposed into two leading EOFs, which together explain 94% of global JJA AOD variance during 1930–2030 (56% for mode 1 and 38% for mode 2). AOD mode 1 increases monotonically over the first half of the record with little change thereafter, in contrast to mode 2 which exhibits sinusoidal behavior, with a positive trend from the mid-1930s to the mid-1970s followed by a steep decline to the early 2020s. Mode 1 features positive AOD anomalies at low latitudes, with regional hotspots in East and South Asia associated with industrial emissions and in tropical South Africa, South America, Indonesia, and Malaysia associated with BMB emissions, accompanied by weak negative AOD anomalies in western Europe and the eastern United States. While mode 2 is characterized by large positive AOD values in western Europe and the eastern United States, juxtaposed against weaker negative values in South and East Asia and eastern Siberia, the two AOD modes are broadly consistent with the "global increase" and "shift" modes reported in prior studies that considered industrial aerosols alone (e.g., Wang and Wen 2022; Shi et al. 2022; Dong et al. 2024).

The ocean-mediated pathway tends to dominate the global large-scale circulation and precipitation responses to both AOD modes, with offsetting contributions from the atmospheric radiative pathway. However, the interplay between the two pathways is complex and regionally dependent, making it difficult to generalize. In contrast, radiative forcing and SST-driven influences are comparable for the NH LSAT response to mode 1 (low-latitude aerosols), whereas for mode 2, radiative forcing dominates. This suggests that low-latitude aerosols can locally perturb terrestrial air temperatures through both pathways, making them efficient in driving regional changes. In contrast, midlatitude aerosols primarily drive in situ surface air temperature changes through the atmospheric radiative pathway. Although midlatitude aerosols exert weaker local impacts, they have high efficacy in driving remote surface air temperature responses, including contributing to global mean surface air temperature (Shindell and Faluvegi 2009; Persad and Caldeira 2018).

The tropical Indo-Pacific and SH circulation responses to AOD mode 1 exemplify how low-latitude aerosols exert both local and remote influences via atmospheric radiative and SST-induced effects. The tropical Indo-Pacific sector displays a distinctive meridional dipole response in precipitation and tropospheric overturning circulation. The latitudinal structure of this response represents a hybrid between the broad cross-equatorial scale resulting from the ocean-mediated pathway associated with remote and local aerosols (Bollasina et al. 2014; Undorf et al. 2018b) and the narrower NH dipolar pattern driven by the atmospheric radiative pathway, which likely reflects the influence of aerosols from adjacent sources [Fig. 5 in Persad (2023)]. In the SH, both the radiatively forced and SST-driven responses produce poleward-propagating Rossby

Unauthenticated | Downloaded 10/07/26 05:58 PM UTC

wave trains emanating from the tropics into the extratropics but with opposite signs. Their largely canceling responses appear to be initiated by tropical diabatic heating anomalies from convection changes over the Sahel and tropical Indian Ocean in response to remote industrial aerosols, along with adiabatic heating anomalies associated with central Africa BMB aerosols in the atmospheric radiative case. These results suggest a potential aerosol-driven tropical–extratropical teleconnection in the SH, though confirmation with linear models or targeted experiments is needed.

Under the transient framework, we showed that the interplay of atmospheric radiative and ocean-mediated effects is neither uniform nor stationary. Radiative effects can exert not only short-lived adjustments but also persistent, decadal-scale influences. This blurs the conventional distinction between "fast" and "slow" responses to radiative forcing, as long-term evolving radiative forcing itself may encompass a slow component (i.e., the radiative response is not a purely fast adjustment in the classical sense). With aerosol emissions expected to decline and clean air legislation already enacted in some countries, it is critical to account for both atmospheric radiative and ocean-mediated components of aerosol effects when predicting regional hydroclimate and risks such as heat extremes, given the mobility and geography-dependent nature of their nuanced interplay.

Much remains to be understood about the mechanisms underlying the atmospheric radiative and ocean-mediated pathways of response to the two AOD modes documented here, including the relative contributions of local versus remote aerosol emissions and their mode dependence, warranting further analysis of our experiments. Our study has utilized one climate model [CESM1 (CAM5)] and one (CMIP5) representation of historical time-evolving industrial and biomass burning aerosols, both of which have known strengths and shortcomings (e.g., Holland et al. 2024). Repeating our approach with other models and updated aerosol emissions inventories (such as the CMIP6 SSPs) would be a useful next step for addressing structural and forcing uncertainty. In particular, different microphysical schemes and associated aerosol–cloud interactions may alter the simulated magnitudes and patterns of aerosol-induced effects, including the SST responses which may affect the ocean-mediated response pathway. For example, it would be valuable to leverage the CESM2 (CAM6) All-Forcing and Single-Forcing Large Ensembles (Simpson et al. 2023) in a CAM6 AMIP framework, given that CESM2 (CAM6) exhibits stronger aerosol–cloud interactions (and a higher equilibrium climate sensitivity) compared to CESM1 (CAM5) as reported in Zelinka et al. (2014), Bacmeister et al. (2020), and Zelinka et al. (2023). More generally, models with improved representation of aerosol microphysical processes and aerosol–cloud interactions, enhanced vertical and horizontal resolution, and interactive wildfire capabilities may be especially worthwhile in this regard. Applying our protocol to regional aerosol forcing experiments such as those conducted as part of the Regional Aerosol Model Intercomparison Project (Wilcox et al. 2023) may yield additional mechanistic insights, although nonlinear interactions between forcings in different regions may complicate the picture (Diao et al. 2025). Additionally, addressing the seasonal dependence of the AOD modes and the responses they elicit would be a worthwhile next step.

Looking forward, anthropogenic aerosol emissions are expected to undergo substantial changes. With continued air quality regulation in Asia and growing industrial activity in tropical regions, the center of aerosol emissions may shift to South Asia, South America, and Africa, though the timing of this transition remains uncertain (Scholten et al. 2024). This shift is especially concerning given the hydrological sensitivity of the tropics and its ability to influence climate worldwide via teleconnections (Smith et al. 2016; Dittuset al. 2021; Liu et al. 2024). Given the critical role of anthropogenic aerosols in shaping historical changes in regional precipitation over densely populated areas (White et al. 2025, manuscript submitted to *Commun. Earth Environ.*), there is an essential need to incorporate information on anticipated near-term and long-term changes in both industrial and biomass burning aerosol emissions into climate projections and risk assessments (Persad et al. 2023). Importantly, understanding the physical pathways by which aerosols impact global climate would not only improve our interpretation of historical climate trends but also enhance the reliability of future projections in a world increasingly shaped by GHGs and shifting aerosol regimes.

Acknowledgments. We thank both anonymous reviewers for their thoughtful and constructive comments and suggestions which led to improvements in this work. This work was supported by funding from the National Science Foundation (NSF) under Award 2235177. This material and the CESM project are based on work supported by the National Center for Atmospheric Research (NCAR), which is a major facility sponsored by the NSF under Cooperative Agreement 1852977. Computations and data storage resources were provided by the Computational and Information Systems Laboratory (CISL) at NCAR.

Data availability statement. The CESM1 CAM5 AMIP single-forcing experiment data will be made available through a NCAR GLOBUS guest collection upon publication. The CESM1 Large Ensemble simulations used in this study are available from http://www.cesm.ucar.edu/experiments/cesm1.1/LE/#single-forcing and http://www.cesm.ucar.edu/projects/community-projects/LENS.

REFERENCES

Allen, R. J., A. T. Evan, and B. B. B. Booth, 2015: Interhemispheric aerosol radiative forcing and tropical precipitation shifts during the late twentieth century. *J. Climate*, **28**, 8219–8246, https://doi.org/10.1175/JCLI-D-15-0148.1.

——, C. Vega, E. Yao, and W. Liu, 2024: Impact of industrial versus biomass burning aerosols on the Atlantic Meridional Overturning Circulation. *npj Climate Atmos. Sci.*, **7**, 58, https://doi.org/10.1038/s41612-024-00602-8.

Unauthenticated | Downloaded 10/07/26 05:58 PM UTC

Ashok, K., Z. Guan, and T. Yamagata, 2003: Influence of the Indian Ocean Dipole on the Australian winter rainfall. *Geophys. Res. Lett.*, **30**, 1821, https://doi.org/10.1029/2003GL017926.

Bacmeister, J. T., and Coauthors, 2020: CO_2 increase experiments using the CESM: Relationship to climate sensitivity and comparison of CESM1 to CESM2. *J. Adv. Model. Earth Syst.*, **12**, e2020MS002120, https://doi.org/10.1029/2020MS002120.

Bala, G., K. Caldeira, and R. Nemani, 2010: Fast versus slow response in climate change: Implications for the global hydrological cycle. *Climate Dyn.*, **35**, 423–434, https://doi.org/10.1007/s00382-009-0583-y.

Bellouin, N., and Coauthors, 2020: Bounding global aerosol radiative forcing of climate change. *Rev. Geophys.*, **58**, e2019RG000660, https://doi.org/10.1029/2019RG000660.

Berbery, E. H., J. Nogués-Paegle, and J. D. Horel, 1992: Wavelike Southern Hemisphere extratropical teleconnections. *J. Atmos. Sci.*, **49**, 155–177, https://doi.org/10.1175/1520-0469(1992)049<0155:WSHET>2.0.CO;2.

Bollasina, M. A., Y. Ming, and V. Ramaswamy, 2011: Anthropogenic aerosols and the weakening of the South Asian summer monsoon. *Science*, **334**, 502–505, https://doi.org/10.1126/science.1204994.

——, ——, ——, M. D. Schwarzkopf, and V. Naik, 2014: Contribution of local and remote anthropogenic aerosols to the twentieth century weakening of the South Asian monsoon. *Geophys. Res. Lett.*, **41**, 680–687, https://doi.org/10.1002/2013GL058183.

Booth, B. B. B., N. J. Dunstone, P. R. Halloran, T. Andrews, and N. Bellouin, 2012: Aerosols implicated as a prime driver of twentieth-century North Atlantic climate variability. *Nature*, **484**, 228–232, https://doi.org/10.1038/nature10946.

Bretherton, C. S., M. Widmann, V. P. Dymnikov, J. M. Wallace, and I. Bladé, 1999: The effective number of spatial degrees of freedom of a time-varying field. *J. Climate*, **12**, 1990–2009, https://doi.org/10.1175/1520-0442(1999)012<1990:TENOSD>2.0.CO;2.

Cai, W., D. Bi, J. Church, T. Cowan, M. Dix, and L. Rotstayn, 2006: Pan-oceanic response to increasing anthropogenic aerosols: Impacts on the Southern Hemisphere oceanic circulation. *Geophys. Res. Lett.*, **33**, L21707, https://doi.org/10.1029/2006GL027513.

——, P. van Rensch, T. Cowan, and H. H. Hendon, 2011: Teleconnection pathways of ENSO and the IOD and the mechanisms for impacts on Australian rainfall. *J. Climate*, **24**, 3910–3923, https://doi.org/10.1175/2011JCLI4129.1.

Chang, P., and Coauthors, 2026: Future extreme precipitation amplified by intensified mesoscale moisture convergence. *Nat. Geosci.*, **19**, 33–41, https://doi.org/10.1038/s41561-025-01859-1.

Chemke, R., and D. Coumou, 2024: Human influence on the recent weakening of storm tracks in boreal summer. *npj Climate Atmos. Sci.*, **7**, 86, https://doi.org/10.1038/s41612-024-00640-2.

Cunningham, C. X., G. J. Williamson, and D. M. Bowman, 2024: Increasing frequency and intensity of the most extreme wildfires on Earth. *Nat. Ecol. Evol.*, **8**, 1420–1425, https://doi.org/10.1038/s41559-024-02452-2.

Dagan, G., P. Stier, and D. Watson-Parris, 2020: Aerosol forcing masks and delays the formation of the North Atlantic warming hole by three decades. *Geophys. Res. Lett.*, **47**, e2020GL090778, https://doi.org/10.1029/2020GL090778.

Delworth, T. L., and K. W. Dixon, 2006: Have anthropogenic aerosols delayed a greenhouse gas-induced weakening of the North Atlantic thermohaline circulation? *Geophys. Res. Lett.*, **33**, L02606, https://doi.org/10.1029/2005GL024980.

DeRepentigny, P., and Coauthors, 2022: Enhanced simulated early 21st century Arctic sea ice loss due to CMIP6 biomass burning emissions. *Sci. Adv.*, **8**, eabo2405, https://doi.org/10.1126/sciadv.abo2405.

Deser, C., and Coauthors, 2020: Isolating the evolving contributions of anthropogenic aerosols and greenhouse gases: A new CESM1 large ensemble community resource. *J. Climate*, **33**, 7835–7858, https://doi.org/10.1175/JCLI-D-20-0123.1.

Diao, C., Y. Xu, A. Hu, and Z. Wang, 2025: Contrasting the roles of regional anthropogenic aerosols from the western and eastern Hemispheres in driving the 1980–2020 Pacific multidecadal variations. *Atmos. Chem. Phys.*, **25**, 2167–2180, https://doi.org/10.5194/acp-25-2167-2025.

Ding, Q., and E. J. Steig, 2013: Temperature change on the Antarctic Peninsula linked to the tropical Pacific. *J. Climate*, **26**, 7570–7585, https://doi.org/10.1175/JCLI-D-12-00729.1.

Dittus, A. J., E. Hawkins, J. I. Robson, D. M. Smith, and L. J. Wilcox, 2021: Drivers of recent North Pacific decadal variability: The role of aerosol forcing. *Earth's Future*, **9**, e2021EF002249, https://doi.org/10.1029/2021EF002249.

Dong, B., L. J. Wilcox, E. J. Highwood, and R. T. Sutton, 2019: Impacts of recent decadal changes in Asian aerosols on the East Asian summer monsoon: Roles of aerosol–radiation and aerosol–cloud interactions. *Climate Dyn.*, **53**, 3235–3256, https://doi.org/10.1007/s00382-019-04698-0.

——, R. T. Sutton, L. Shaffrey, and B. Harvey, 2022: Recent decadal weakening of the summer Eurasian westerly jet attributable to anthropogenic aerosol emissions. *Nat. Commun.*, **13**, 1148, https://doi.org/10.1038/s41467-022-28816-5.

Dong, Y., J. E. Kay, C. Deser, A. Capotondi, and S. C. Sanchez, 2024: Distilling the evolving contributions of anthropogenic aerosols and greenhouse gases to large-scale low-frequency surface ocean changes over the past century. *Geophys. Res. Lett.*, **51**, e2024GL112020, https://doi.org/10.1029/2024GL112020.

England, M. R., I. Eisenman, N. J. Lutsko, and T. J. Wagner, 2021: The recent emergence of Arctic amplification. *Geophys. Res. Lett.*, **48**, e2021GL094086, https://doi.org/10.1029/2021GL094086.

Fasullo, J. T., J. F. Lamarque, C. Hannay, N. Rosenbloom, S. Tilmes, P. DeRepentigny, A. Jahn, and C. Deser, 2022: Spurious late historical-era warming in CESM2 driven by prescribed biomass burning emissions. *Geophys. Res. Lett.*, **49**, e2021GL097420, https://doi.org/10.1029/2021GL097420.

Gillett, Z. E., H. H. Hendon, J. M. Arblaster, H. Lin, and D. Fuchs, 2022: On the dynamics of Indian Ocean teleconnections into the Southern Hemisphere during austral winter. *J. Atmos. Sci.*, **79**, 2453–2469, https://doi.org/10.1175/JAS-D-21-0206.1.

Gregory, J. M., and Coauthors, 2004: A new method for diagnosing radiative forcing and climate sensitivity. *Geophys. Res. Lett.*, **31**, L03205, https://doi.org/10.1029/2003GL018747.

He, J., and B. J. Soden, 2015: Anthropogenic weakening of the tropical circulation: The relative roles of direct CO_2 forcing and sea surface temperature change. *J. Climate*, **28**, 8728–8742, https://doi.org/10.1175/JCLI-D-15-0205.1.

Heyblom, K. B., H. A. Singh, P. J. Rasch, and H. Hirasawa, 2023: Variability in biomass burning emissions weakens aerosol forcing due to nonlinear aerosol-cloud interactions. *Geophys. Res. Lett.*, **50**, e2022GL102685, https://doi.org/10.1029/2022GL102685.

Unauthenticated | Downloaded 10/07/26 05:58 PM UTC

Hill, S. A., Y. Ming, and I. M. Held, 2015: Mechanisms of forced tropical meridional energy flux change. *J. Climate*, **28**, 1725–1742, https://doi.org/10.1175/JCLI-D-14-00165.1.

Hirasawa, H., P. J. Kushner, M. Sigmond, J. Fyfe, and C. Deser, 2020: Anthropogenic aerosols dominate forced multidecadal Sahel precipitation change through distinct atmospheric and oceanic drivers. *J. Climate*, **33**, 10187–10204, https://doi.org/10.1175/JCLI-D-19-0829.1.

Holland, M. M., and Coauthors, 2024: New model ensemble reveals how forcing uncertainty and model structure alter climate simulated across CMIP generations of the Community Earth System Model. *Geosci. Model Dev.*, **17**, 1585–1602, https://doi.org/10.5194/gmd-17-1585-2024.

Hoskins, B. J., and T. Ambrizzi, 1993: Rossby wave propagation on a realistic longitudinally varying flow. *J. Atmos. Sci.*, **50**, 1661–1671, https://doi.org/10.1175/1520-0469(1993)050<1661:RWPOAR>2.0.CO;2.

Hua, W., A. Dai, L. Zhou, M. Qin, and H. Chen, 2019: An externally forced decadal rainfall seesaw pattern over the Sahel and southeast Amazon. *Geophys. Res. Lett.*, **46**, 923–932, https://doi.org/10.1029/2018GL081406.

——, S. Lou, X. Huang, L. Xue, K. Ding, Z. Wang, and A. Ding, 2024: Diagnosing uncertainties in global biomass burning emission inventories and their impact on modeled air pollutants. *Atmos. Chem. Phys.*, **24**, 6787–6807, https://doi.org/10.5194/acp-24-6787-2024.

Hwang, Y.-T., D. M. W. Frierson, and S. M. Kang, 2013: Anthropogenic sulfate aerosol and the southward shift of tropical precipitation in the late 20th century. *Geophys. Res. Lett.*, **40**, 2845–2850, https://doi.org/10.1002/grl.50502.

——, S.-P. Xie, P.-J. Chen, H.-Y. Tseng, and C. Deser, 2024: Contribution of anthropogenic aerosols to persistent La Niña-like conditions in the early 21st century. *Proc. Natl. Acad. Sci. USA*, **121**, e2315124121, https://doi.org/10.1073/pnas.2315124121.

IPCC, 2021: Short-lived climate forcers. *Climate Change 2021: The Physical Science Basis*, V. Masson-Delmotte et al., Eds., Cambridge University Press, 817–922, https://doi.org/10.1017/9781009157896.008.

Kang, J. M., T. A. Shaw, and L. Sun, 2024: Anthropogenic aerosols have significantly weakened the regional summertime circulation in the Northern Hemisphere during the satellite era. *AGU Adv.*, **5**, e2024AV001318, https://doi.org/10.1029/2024AV001318.

Kang, S. M., S.-P. Xie, C. Deser, and B. Xiang, 2021: Zonal mean and shift modes of historical climate response to evolving aerosol distribution. *Sci. Bull.*, **66**, 2405–2411, https://doi.org/10.1016/j.scib.2021.07.013.

Kay, J. E., and Coauthors, 2015: The Community Earth System Model (CESM) large ensemble project: A community resource for studying climate change in the presence of internal climate variability. *Bull. Amer. Meteor. Soc.*, **96**, 1333–1349, https://doi.org/10.1175/BAMS-D-13-00255.1.

Lamarque, J.-F., and Coauthors, 2010: Historical (1850–2000) gridded anthropogenic and biomass burning emissions of reactive gases and aerosols: Methodology and application. *Atmos. Chem. Phys.*, **10**, 7017–7039, https://doi.org/10.5194/acp-10-7017-2010.

Lawrence, D. M., and Coauthors, 2011: Parameterization improvements and functional and structural advances in version 4 of the Community Land Model. *J. Adv. Model. Earth Syst.*, **3**, M03001, https://doi.org/10.1029/2011MS00045.

Li, S., W. Liu, R. J. Allen, J.-R. Shi, and L. Li, 2023: Ocean heat uptake and interbasin redistribution driven by anthropogenic aerosols and greenhouse gases. *Nat. Geosci.*, **16**, 695–703, https://doi.org/10.1038/s41561-023-01219-x.

Li, X., M. Ting, and D. E. Lee, 2018: Fast adjustments of the Asian summer monsoon to anthropogenic aerosols. *Geophys. Res. Lett.*, **45**, 1001–1010, https://doi.org/10.1002/2017GL076667.

——, ——, Y. You, D.-E. Lee, D. M. Westervelt, and Y. Ming, 2020: South Asian summer monsoon response to aerosol-forced sea surface temperatures. *Geophys. Res. Lett.*, **47**, e2019GL085329, https://doi.org/10.1029/2019GL085329.

——, and Coauthors, 2021: Tropical teleconnection impacts on Antarctic climate changes. *Nat. Rev. Earth Environ.*, **2**, 680–698, https://doi.org/10.1038/s43017-021-00204-5.

Li, Y., J. Li, F. F. Jin, and S. Zhao, 2015: Interhemispheric propagation of stationary Rossby waves in a horizontally nonuniform background flow. *J. Atmos. Sci.*, **72**, 3233–3256, https://doi.org/10.1175/JAS-D-14-0239.1.

Liu, F., and Coauthors, 2024: Increased Asian aerosols drive a slowdown of Atlantic Meridional Overturning Circulation. *Nat. Commun.*, **15**, 18, https://doi.org/10.1038/s41467-023-44597-x.

Liu, L., and Coauthors, 2018: A PDRMIP multimodel study on the impacts of regional aerosol forcings on global and regional precipitation. *J. Climate*, **31**, 4429–4447, https://doi.org/10.1175/JCLI-D-17-0439.1.

Liu, X., and Coauthors, 2012: Toward a minimal representation of aerosols in climate models: Description and evaluation in the Community Atmosphere Model CAM5. *Geosci. Model Dev.*, **5**, 709–739, https://doi.org/10.5194/gmd-5-709-2012.

Lund, M. T., G. Myhre, and B. H. Samset, 2019: Anthropogenic aerosol forcing under the shared socioeconomic pathways. *Atmos. Chem. Phys.*, **19**, 13827–13839, https://doi.org/10.5194/acp-19-13827-2019.

Meehl, G. A., and Coauthors, 2013: Climate change projections in CESM1 (CAM5) compared to CCSM4. *J. Climate*, **26**, 6287–6308, https://doi.org/10.1175/JCLI-D-12-00572.1.

Menary, M. B., and Coauthors, 2020: Aerosol-forced AMOC changes in CMIP6 historical simulations. *Geophys. Res. Lett.*, **47**, e2020GL088166, https://doi.org/10.1029/2020GL088166.

Ming, Y., and V. Ramaswamy, 2011: A model investigation of aerosol-induced changes in tropical circulation. *J. Climate*, **24**, 5125–5133, https://doi.org/10.1175/2011JCLI4108.1.

Morrison, H., and A. Gettelman, 2008: A new two-moment bulk stratiform cloud microphysics scheme in the Community Atmosphere Model, version 3 (CAM3). Part I: Description and numerical tests. *J. Climate*, **21**, 3642–3659, https://doi.org/10.1175/2008JCLI2105.1.

Mueller, B. L., N. P. Gillett, A. H. Monahan, and F. W. Zwiers, 2018: Attribution of Arctic sea ice decline from 1953 to 2012 to influences from natural, greenhouse gas, and anthropogenic aerosol forcing. *J. Climate*, **31**, 7771–7787, https://doi.org/10.1175/JCLI-D-17-0552.1.

Nabat, P., and Coauthors, 2025: Multi-model assessment of the role of anthropogenic aerosols in summertime climate change in Europe. *Geophys. Res. Lett.*, **52**, e2024GL112474, https://doi.org/10.1029/2024GL112474.

Neale, R. B., and Coauthors, 2010: Description of the NCAR Community Atmosphere Model (CAM 5.0). NCAR Tech. Note NCAR/TN-486+STR, 268 pp.

North, G. R., T. L. Bell, R. F. Cahalan, and F. J. Moeng, 1982: Sampling errors in the estimation of Empirical Orthogonal

Unauthenticated | Downloaded 10/07/26 05:58 PM UTC

Functions. *Mon. Wea. Rev.*, **110**, 699–706, https://doi.org/10.1175/1520-0493(1982)110<0699:SEITEO>2.0.CO;2.

Persad, G. G., 2023: The dependence of aerosols' global and local precipitation impacts on the emitting region. *Atmos. Chem. Phys.*, **23**, 3435–3452, https://doi.org/10.5194/acp-23-3435-2023.

——, and K. Caldeira, 2018: Divergent global-scale temperature effects from identical aerosols emitted in different regions. *Nat. Commun.*, **9**, 3289, https://doi.org/10.1038/s41467-018-05838-6.

——, D. J. Paynter, Y. Ming, and V. Ramaswamy, 2017: Competing atmospheric and surface-driven impacts of absorbing aerosols on the East Asian summertime climate. *J. Climate*, **30**, 8929–8949, https://doi.org/10.1175/JCLI-D-16-0860.1.

——, and Coauthors, 2023: Rapidly evolving aerosol emissions are a dangerous omission from near-term climate risk assessments. *Environ. Res.: Climate*, **2**, 032001, https://doi.org/10.1088/2752-5295/acd6af.

Rodgers, K. B., and Coauthors, 2021: Ubiquity of human-induced changes in climate variability. *Earth Syst. Dyn.*, **12**, 1393–1411, https://doi.org/10.5194/esd-12-1393-2021.

Roesch, C. M., E. Fons, A. P. Ballinger, J. Runge, and G. C. Hegerl, 2025: Decreasing aerosols increase the European summer diurnal temperature range. *npj Climate Atmos. Sci.*, **8**, 47, https://doi.org/10.1038/s41612-025-00922-3.

Samset, B. H., and Coauthors, 2016: Fast and slow precipitation responses to individual climate forcers: A PDRMIP multimodel study. *Geophys. Res. Lett.*, **43**, 2782–2791, https://doi.org/10.1002/2016GL068064.

Scholten, R. C., S. Veraverbeke, Y. Chen, and J. T. Randerson, 2024: Spatial variability in Arctic–boreal fire regimes influenced by environmental and human factors. *Nat. Geosci.*, **17**, 866–873, https://doi.org/10.1038/s41561-024-01505-2.

Schumacher, D. L., J. Singh, M. Hauser, E. M. Fischer, M. Wild, and S. I. Seneviratne, 2024: Exacerbated summer European warming not captured by climate models neglecting long-term aerosol changes. *Commun. Earth Environ.*, **5**, 182, https://doi.org/10.1038/s43247-024-01332-8.

Shaw, T., and A. Voigt, 2015: Tug of war on summertime circulation between radiative forcing and sea surface warming. *Nat. Geosci.*, **8**, 560–566, https://doi.org/10.1038/ngeo2449.

Shawki, D., A. Voulgarakis, A. Chakraborty, M. Kasoar, and J. Srinivasan, 2018: The South Asian monsoon response to remote aerosols: Global and regional mechanisms. *J. Geophys. Res. Atmos.*, **123**, 11 585–11 601, https://doi.org/10.1029/2018JD028623.

Shi, J., Y. Kwon, and S. E. Wijffels, 2022: Two distinct modes of climate responses to the anthropogenic aerosol forcing changes. *J. Climate*, **35**, 3445–3457, https://doi.org/10.1175/JCLI-D-21-0656.1.

Shindell, D., and G. Faluvegi, 2009: Climate response to regional radiative forcing during the twentieth century. *Nat. Geosci.*, **2**, 294–300, https://doi.org/10.1038/ngeo473.

Simpson, I. R., and Coauthors, 2023: The CESM2 single-forcing large ensemble and comparison to CESM1: Implications for experimental design. *J. Climate*, **36**, 5687–5711, https://doi.org/10.1175/JCLI-D-22-0666.1.

Smith, D. M., and Coauthors, 2016: Role of volcanic and anthropogenic aerosols in the recent global surface warming slowdown. *Nat. Climate Change*, **6**, 936–940, https://doi.org/10.1038/nclimate3058.

Takemura, T., 2012: Distributions and climate effects of atmospheric aerosols from the preindustrial era to 2100 along Representative Concentration Pathways (RCPs) simulated using the global aerosol model SPRINTARS. *Atmos. Chem. Phys.*, **12**, 11 555–11 572, https://doi.org/10.5194/acp-12-11555-2012.

Tian, Y., S. Hu, and C. Deser, 2023: Critical role of biomass burning aerosols in enhanced historical Indian Ocean warming. *Nat. Commun.*, **14**, 3508, https://doi.org/10.1038/s41467-023-39204-y.

Undorf, S., M. A. Bollasina, and G. C. Hegerl, 2018a: Impacts of the 1900–74 increase in anthropogenic aerosol emissions from North America and Europe on Eurasian summer climate. *J. Climate*, **31**, 8381–8399, https://doi.org/10.1175/JCLI-D-17-0850.1.

——, D. Polson, M. A. Bollasina, Y. Ming, A. Schurer, and G. C. Hegerl, 2018b: Detectable impact of local and remote anthropogenic aerosols on the 20th century changes of West African and South Asian monsoon precipitation. *J. Geophys. Res. Atmos.*, **123**, 4871–4889, https://doi.org/10.1029/2017JD027711.

van der Werf, G. R., and Coauthors, 2017: Global fire emissions estimates during 1997–2016. *Earth Syst. Sci. Data*, **9**, 697–720, https://doi.org/10.5194/essd-9-697-2017.

Wang, H., and Y.-J. Wen, 2022: Climate response to the spatial and temporal evolutions of anthropogenic aerosol forcing. *Climate Dyn.*, **59**, 1579–1595, https://doi.org/10.1007/s00382-021-06059-2.

——, S.-P. Xie, Y. Kosaka, Q. Liu, and Y. Du, 2019: Dynamics of Asian summer monsoon response to anthropogenic aerosol forcing. *J. Climate*, **32**, 843–858, https://doi.org/10.1175/JCLI-D-18-0386.1.

——, and Coauthors, 2024: Atmosphere teleconnections from abatement of China aerosol emissions exacerbate Northeast Pacific warm blob events. *Proc. Natl. Acad. Sci. USA*, **121**, e2313797121, https://doi.org/10.1073/pnas.2313797121.

Wang, Z., and Coauthors, 2021: Incorrect Asian aerosols affecting the attribution and projection of regional climate change in CMIP6 models. *npj Climate Atmos. Sci.*, **4**, 2, https://doi.org/10.1038/s41612-020-00159-2.

Westervelt, D. M., Y. You, X. Li, M. Ting, D. E. Lee, and Y. Ming, 2020: Relative importance of greenhouse gases, sulfate, organic carbon, and black carbon aerosol for South Asian monsoon rainfall changes. *Geophys. Res. Lett.*, **47**, e2020GL088363, https://doi.org/10.1029/2020GL088363.

Wilcox, L. J., and Coauthors, 2023: The Regional Aerosol Model Intercomparison Project (RAMIP). *Geosci. Model Dev.*, **16**, 4451–4479, https://doi.org/10.5194/gmd-16-4451-2023.

Wilks, D. S., 2016: "The stippling shows statistically significant grid points": How research results are routinely overstated and overinterpreted, and what to do about it. *Bull. Amer. Meteor. Soc.*, **97**, 2263–2273, https://doi.org/10.1175/BAMS-D-15-00267.1.

Xiang, B., S.-P. Xie, S. M. Kang, and R. J. Kramer, 2023: An emerging Asian aerosol dipole pattern reshapes the Asian summer monsoon and exacerbates Northern Hemisphere warming. *npj Climate Atmos. Sci.*, **6**, 77, https://doi.org/10.1038/s41612-023-00400-8.

Xie, S.-P., B. Lu, and B. Xiang, 2013: Similar spatial patterns of climate responses to aerosol and greenhouse gas changes. *Nat. Geosci.*, **6**, 828–832, https://doi.org/10.1038/ngeo1931.

Zelinka, M. D., T. Andrews, P. M. Forster, and K. E. Taylor, 2014: Quantifying components of aerosol-cloud-radiation interactions in climate models. *J. Geophys. Res. Atmos.*, **119**, 7599–7615, https://doi.org/10.1002/2014JD021710.

Unauthenticated | Downloaded 10/07/26 05:58 PM UTC

——, C. J. Smith, Y. I. Qin, and K. E. Taylor, 2023: Comparison of methods to estimate aerosol effective radiative forcings in climate models. *Atmos. Chem. Phys.*, **23**, 8879–8898, https://doi.org/10.5194/acp-23-8879-2023.

Zhang, Y., and Coauthors, 2021: Impacts of emission changes in China from 2010 to 2017 on domestic and intercontinental air quality and health effect. *Atmos. Chem. Phys.*, **21**, 16 051–16 065, https://doi.org/10.5194/acp-21-16051-2021.

Unauthenticated | Downloaded 10/07/26 05:58 PM UTC